Mon. Not. R. Astron. Soc. **000**, 000–000 (0000) Printed 5 February 2008 (MN LATEX style file v2.2)

A study of the SZ increment using SCUBA

Michael Zemcov[1,2], Colin Borys[3], Mark Halpern[2], Philip Mauskopf[1], Douglas Scott[2]

[1] *School of Physics & Astronomy, Cardiff University, Cardiff, Wales CF24 3YB, UK*
[2] *Department of Physics & Astronomy, University of British Columbia, Vancouver, BC V6T 1Z1, Canada*
[3] *Department of Astronomy & Astrophysics, University of Toronto, Toronto, ON M5S 3H8, Canada*

arXiv:astro-ph/0612708v2 2 May 2007

Accepted 2006 December 19. Received 2006 December 1; in original form 2006 June 30

ABSTRACT

In a search for evidence of the short wavelength increment in the Sunyaev–Zel'dovich (SZ) effect, we have analyzed archival galaxy cluster data from the Sub-millimetre Common User Bolometer Array (SCUBA) on the James Clerk Maxwell Telescope, resulting in the most complete pointed survey of clusters at $850\,\mu$m to date. SCUBA's $850\,\mu$m passband overlaps the peak of the SZ increment. The sample consists of 44 galaxy clusters in the range $0 < z < 1.3$. Maps of each of the clusters have been made and sources have been extracted; as an ancillary product we generate the most thorough galaxy cluster point source list yet from SCUBA. Seventeen of these clusters are free of obvious AGN and have data deep enough to provide interesting measurements of the expected SZ signal. Specialized analysis techniques are employed to extract the SZ effect signal from these SCUBA data, including using SCUBA's short wavelength band as an atmospheric monitor and fitting the long wavelength channel to a model of the spatial distribution of each cluster's SZ effect. By explicitly excising the exact cluster centre from our analysis we demonstrate that emission from galaxies within the cluster does not contaminate our measurement. The SZ amplitudes from our measurements are consistently higher than the amplitudes inferred from low frequency measurements of the SZ decrement.

Key words: cosmology: cosmic microwave background – cosmology: observations – galaxies: clusters: general – submillimetre

1 INTRODUCTION

The Sunyaev–Zel'dovich (SZ) effect (Sunyaev & Zel'dovich 1972) is a distortion of the cosmic microwave background (CMB) spectrum seen through a reservoir of hot plasma such as is found in clusters of galaxies. Measurements of the SZ effect in clusters can be used to determine the physical conditions within the intracluster medium. The SZ amplitude, in combination with other data, can act as an important probe of cosmology (Birkinshaw 1999, Carlstrom, Holder & Reese 2002).

There are several motivations for measuring the SZ effect. Blank field searches for clusters at all redshifts allow one to constrain the cluster redshift distribution $N(z)$. This is anticipated to be especially important in understanding the epoch of early cluster formation since the SZ effect remains bright at large redshifts. These studies provide information about the massive end of the distribution of collapsed objects in the Universe. Surveys of catalogues of known clusters allow one to measure large scale flows via the kinetic SZ effect. This effect is small in any single cluster so larger surveys are called for. Unlike the intrinsic SZ effect, the kinetic effect is spectrally broad and can be either positive or negative, so measurement over a wide frequency range is desirable. In principle, a combination of the data presented here and SZ measurements at other frequencies provide a measurement of the kinetic SZ effect, although in practice this is quite difficult, even with measurements at a number of wavelengths (Benson et al. 2004). Detailed targeted observations of a single cluster allow the study of physical details of the baryon distribution and dynamics in the cluster, especially in conjunction with good X-ray maps. These motivations are all discussed in, for example, Carlstrom, Holder & Reese (2002).

SZ decrement measurements at frequencies of tens of GHz now seem almost routine. However, detection of the increment has proven to be considerably more difficult. The data discussed here can be used to address the physical parameters of clusters on an individual basis, and are especially powerful when combined with data at several other wavelengths (LaRoque et al. 2006). Such combinations exploit the characteristic spectral shape of the SZ effect to increase the confidence of the overall measurement, and perhaps to constrain smaller spectral modifications, i.e. from the kinetic SZ effect. Of practical interest, these archival SZ effect measurements provide insight into the practical difficulties associated with measurement of low surface brightness, extended emission in the mm/sub-mm regime.

Ground based sub-millimetre (sub-mm) observations of the SZ increment are possible because the peak of the SZ spectral distortion occurs near $370\,$GHz ($810\,\mu$m) in an atmospheric window.

© 0000 RAS

However, while decrements in emission are rare astrophysically and can be ascribed to the SZ effect with little ambiguity, the sub-mm emission from clusters might not be due to the SZ effect alone. Three possible contributions to the flux are:

(i) the SZ effect itself,
(ii) gravitational lensing of high redshift background sub-mm sources, and
(iii) dust–obscured starburst galaxies within the cluster itself.

Despite being foregrounds from the point of view of SZ effect measurement, items (ii) and (iii) are interesting topics in their own right. Although gravitationally lensed background sources offer little information about the lensing cluster itself (besides a constraint on the mass surface density in the lens), they allow important measurements of high redshift sub-mm sources which would otherwise be too dim to resolve. Virtually all massive galaxy clusters which have been studied host at least one strongly lensed sub-mm source. Several studies have made use of galaxy clusters as natural telescopes to probe the high redshift sub-mm population (e.g. Smail et al. 1997, Chapman et al. 2002, Best 2002, Cowie, Barger & Kneib 2002, Smail et al. 2002). Sub-mm sources within a galaxy cluster are rare and, when present, tend to be associated with an AGN in the central cluster galaxy (e.g. Edge et al. 1999, Chapman et al. 2002). There are weaker but more problematic effects due to increased incidence of dusty star-forming galaxies at higher redshifts (see e.g. Best 2002, Webb et al. 2005), perhaps related to the Butcher-Oemler type phenomenon seen outside the cores of some clusters in mid-IR studies (e.g. Duc et al. 2002). As discussed later, both lensed sources and emission from galaxies in the clusters themselves are problematic foregrounds and provide some of the fundamental limitations to measuring the SZ increment.

SCUBA on the JCMT, which began common-user operations in 1997, has the most extensive archive of sub-mm measurements of galaxy clusters available. We have attempted to measure the SZ effect increment in these clusters using this data set following the techniques we developed in an earlier paper (Zemcov et al. 2003). Previous analyses of these data have been performed by several different groups, and so have been quite heterogeneous in terms of the analysis methods employed. In contrast, this paper presents the results of using a consistent analysis pipeline for these galaxy cluster data. In particular we take great care to remove the effects of common mode atmospheric emission in a way which does not also cancel the SZ emission. By addressing both source identification and the SZ effect, and by handling all of the data consistently, we have produced a uniformly selected list of candidate sources in these cluster fields.

In this paper, we first present the data selection procedure and data analysis leading to the individual cluster maps. This is followed by a presentation of the SZ effect analysis method and results. The point source list and SZ effect amplitude results are then discussed. Finally, we discuss some of the difficulties associated with SZ increment measurement in the presence of strong atmospheric emission and lensed background sources, and lessons learned for future experiments. This paper also contains 3 appendices: the first presents listings of integration times and weather conditions for each cluster field; the second presents a complete list of point sources; and the third is a discussion of the characteristics of each cluster, with a list of references for relevant prior work on each cluster field.

2 DATA COLLECTION & ANALYSIS

This work has made use of both JCMT archival data and new JCMT observations; both are discussed in detail below, followed by a description of our analysis methods, which differ from standard SCUBA analysis tools. These methods follow those described in Zemcov et al. (2003) to which the reader is directed for more detail. Essentially, this analysis differs from the canonical SCUBA pipeline in two major ways. Firstly, SCUBA's short wavelength channel is used to subtract atmospheric contamination from the long wavelength (science) channel. Secondly, we fit the set of double difference measurements to a model of the SZ effect rather than attempting to image it directly. The motivation for these steps is to account for loss of flux due to SCUBA's spatial differencing and standard 'sky-removal' techniques. Before attempting to measure the SZ signal we identify and remove contaminating point sources.

2.1 Archival data selection

A candidate cluster list has been compiled as follows. Firstly, the list of proposal titles and abstracts submitted to the JCMT over the period 1997 to 2005 was searched for projects likely to target galaxy clusters and the target lists of these proposals was examined. This forms the core of our target list. In addition, the literature was searched for published SCUBA observations of galaxy clusters; the list of clusters found in this way completely overlaps with the proposal list. The final check is to find the complete target list for any project that targeted even a single galaxy cluster, which should find essentially all unpublished observations. Only unpublished observations of cluster fields from projects whose proposed observation programme was unrelated to galaxy cluster measurements will be missed using these search criteria.

The on-line JCMT archives[1] were searched for data collected within a 10 arcmin box centered on the candidate SZ clusters. Almost all SCUBA galaxy cluster data taken in unpolarized 'jiggle mapping' mode (Holland et al. 1999, Archibald et al. 2002, Zemcov et al. 2003) between SCUBA's commissioning in 1997 and retirement in 2005 are considered for analysis [2]. SCUBA uses two jiggle mapping modes: 16 point, which fully samples only the $850\ \mu$m array; and 64 point, which fully samples both the long and short wavelength arrays. Either sampling mode can be used here, although because the $450\ \mu$m array data is used as an atmospheric monitor, data sets where the data from the short wavelength array were not recorded cannot be used (this only occurred in approximately 1 per cent of the data). Those data sets which were flagged as 'aborted' during the observation may have major defects (incorrect telescope pointing, focusing errors, etc.) and are checked and rejected if necessary at this stage. A summary of those data sets which pass these initial criteria are given in Appendix A.

2.2 New Cl 0152.7−1357 observations

The work of Zemcov et al. (2003) showed that heterogeneous chopping patterns make SZ effect measurements with SCUBA very difficult. To test our ideas about optimizing SZ effect measurement

[1] `http://cadcwww.hia.nrc.ca/jcmt/`
[2] The only clusters which have been excluded are those studied as part of the Red Cluster Survey (Gladders & Yee 2005); these currently have little supporting SZ decrement and X-ray data, making it difficult to construct a model for their expected SZ effect brightness distribution.

with a spatially chopped instrument like SCUBA, new observations of a high redshift galaxy cluster were performed using a chopping strategy designed to optimize the signal from the cluster's SZ effect increment. These new JCMT data were obtained on Sept. 28, 29 and Oct. 17, 2003. The target of these observations was Cl $0152.7-1357$, the most distant cluster in the *ROSAT* galaxy cluster catalogue. This particular cluster was chosen for new observations because it lies at high redshift and, due to its X-ray brightness, is well studied at other wavelengths. Cl $0152-1357$ was originally discovered in the Wide Angle *ROSAT* Pointed Survey (WARPS; Scharf et al. 1997), and independently in the *ROSAT* Deep Cluster Survey (RDCS; Rosati et al. 1998) and Serendipitous High-Redshift Archival Cluster (SHARC) samples (Romer et al. 2000). Joy et al. (2001) have previously detected the SZ effect decrement in this cluster. More recently, Maughan et al. (2003) observed this cluster with *Chandra*, and found that it is resolvable into northern and southern 'clumps' of X-ray emission. The southern clump's X-ray emission is highly peaked, which makes unambiguous determination of the SZ effect in this cluster difficult. Therefore, our observations focused on the northern clump, centred at $\alpha_{\rm J2000} = 1^{\rm h}52^{\rm m}44.^{\rm s}2$, $\delta_{\rm J2000} = -13^\circ57'16''$ (Maughan et al. 2003). The data were taken in a similar manner to those discussed in Zemcov et al. (2003). A 16 point jiggle pattern with multiple chop throws and orientations was used to sample the spatial region around this cluster. As chopping onto the southern clump would be highly undesirable, the chops were carefully selected to avoid this region. The average optical depth as measured by the JCMT water vapour monitor (WVM, Wiedner et al. 2001) during these observations was $\tau_{850} = 0.225$. In all, 13.4 ks of data were taken for this field.

2.3 Preliminary analysis & calibration

The data are first double–differenced and flat–fielded using the standard SURF analysis package[3]. Double–differencing involves subtracting the data between the two nod positions to remove both long term drifts in the data (Holland et al. 1999) and a systematic effect which may be due to differential illumination (Zemcov et al. 2005). Fortunately, none of the data discussed here suffer from the 16 sample correlated noise effect noted by Borys et al. (2004) and subsequently discussed by Zemcov et al. (2005) and Webb et al. (2005), so we can proceed without correction. The flat–fielding procedure multiplies the data from each bolometer by a known amount to account for variation between detectors; the multiplicative values are very stable in SCUBA data (T. Jenness, private communication).

Next, the SURF package is used to correct the data for atmospheric extinction. This involves multiplying each bolometer's time series by $e^{\tau_{850}A}$, where A is the airmass of the pointing. τ_{850} is found from either the CSO τ–meter data provided in the JCMT archive, using the relationships between $\tau_{220\,\rm GHz}$ and $\tau_{350\,\rm GHz}$ provided in Archibald et al. (2002), or archival skydips should the τ-meter data be unavailable. The data from each bolometer are then de-spiked by removing points greater than 5σ away from the mean of the time stream.

Because these data sets sometimes involve observations of the same field performed under very different conditions with different observational strategies, in some cases separated by as much as 5 years, calibration is a concern. The data for each observation are calibrated at this stage by multiplying each time series by a flux conversion factor (FCF). For every night in our data set, we retrieve all the calibration observations of Mars, Uranus, CRL 618, HL Tau or CRL 2688, which are the best non-variable calibrators available to SCUBA (Jenness et al. 2002). An $850\,\mu$m FCF is derived from each of these observations, using the peak flux method discussed in Jenness et al. (2002). Planet brightnesses are derived using the FLUXES package (Privett, Jenness & Matthews 1998), while the secondary calibrators' fluxes are given in Jenness et al. (2002).

The FCF chosen for each data set is generally that derived from the calibration observation closest in time to the observation of interest. However, because focusing the telescope tends to change the calibration somewhat (T. Jenness, private communication), a calibration observation performed right after a focusing is not applied to data taken before that focusing. This helps to ensure that data and calibration were both taken with the same optical configuration. In cases where no calibrations are available, the fiducial FCFs given in Jenness et al. (2002) are applied to the data. The set of calibrations used here have statistics very similar to those presented in Jenness et al. (2002).

2.4 Residual atmospheric emission removal

Bolometers in the SCUBA array each have their own noise properties, and these must be checked from night to night. As is commonly done, we remove the noisiest bolometers in the array from analysis. For each data file, individual bolometers with time-stream variances larger than η times the average bolometer variance at a given wavelength are removed from the analysis pipeline; in this analysis, $\eta = 1.5$. While this value of η may appear to be surprisingly low, because the very noisiest bolometers dominate the variance $\eta \simeq 1$ does *not* imply we are removing half of the bolometers. Typically only between 2 and 7 of 37 bolometers for a given data subset are removed for this η. Although we could perform an iterative procedure (with a larger value of η) to remove bolometers based on a recalculated average variance, we find that this is unnecessary.

Thermal emission from both the atmosphere and telescope's surroundings contribute a large spurious signal at sub-mm wavelengths. The double–differencing scheme SCUBA employs reduces much of this signal, but atmospheric effects still persist, mainly as a common-mode noise across the array. It is standard practice to subtract the array average at each time step to remove these residual signals (Holland et al. 1999). Unfortunately, the SZ profile is appreciable compared to the array size. This means that removing the $850\,\mu$m array average at each time step would remove a non-negligible amount of the SZ signal in these data sets. Fortunately, the atmospheric noise is strongly correlated between the arrays at both wavelengths (Holland et al. 1999, Borys, Chapman, & Scott 1999, Jenness et al. 2002). Therefore, we can use the $450\,\mu$m time stream to subtract the common–mode atmospheric contribution from the $850\,\mu$m time stream; this is accomplished as follows. Denote the time series at wavelength λ as $R_b^\lambda(t)$, where $\lambda \in \{450\,\mu{\rm m}, 850\,\mu{\rm m}\}$, b is an index running over bolometers and t is time. The $450\,\mu$m and $850\,\mu$m array averages, denoted $\langle R^\lambda(t)\rangle$, are calculated at each time step. Because double–differenced SCUBA data retains some arbitrary instrumental offset in its time series at each wavelength, we also calculate the DC offset of both time se-

[3] For details on the implementation of these procedures, see `http://www.starlink.rl.ac.uk/star/docs/sun216.htx/sun216.html`.

ries, $\overline{R^\lambda}$, via

$$\overline{R^\lambda} = \frac{1}{T}\sum_{t=0}^{T} R^\lambda(t), \quad (1)$$

where T is the length of time in the data subset under consideration. The data series $M^{450}(t) = \langle R^{450}(t)\rangle - \overline{R^{450}}$ is then formed, and is fit to $\langle R^{850}(t)\rangle$ to obtain a multiplicative scaling factor, α. An atmosphere subtracted $850\,\mu$m time series, $S_b^{850}(t)$, is then calculated via:

$$S_b^{850}(t) = R_b^{850}(t) - \alpha\langle R^{450}(t)\rangle - \overline{R^{850}}, \quad (2)$$

as discussed in Borys, Chapman, & Scott (1999) and Zemcov et al. (2003). This $S_b^{850}(t)$ is the final, cleaned time series used in the analysis. The value of α does not vary by more than 10 per cent over a night, but does vary considerably on time scales of months.

Both Borys, Chapman, & Scott (1999) and Archibald et al. (2002) discuss the correlation between the bolometer-averaged time streams of SCUBA's $450\,\mu$m and $850\,\mu$m arrays in some detail. However, the effectiveness of using the $450\,\mu$m atmosphere removal method for large data sets has not been considered in previous work. As such an investigation is critical to understanding the errors in our SZ estimates, we perform a new analysis here.

The variance of the time stream of each file[4] is calculated after double–differencing, extinction correction, etc., but *before* any array average has been removed; this is termed the 'raw' variance, $\sigma^2_{\rm raw}$. Atmospheric removal using the array averages at each time step is then implemented using either the $850\,\mu$m array average (i.e. the standard SURF) method, or the fit to the $450\,\mu$m array average method (Eq. 2). The variances of these 'atmosphere subtracted' time streams (denoted by σ^2_{-850} and σ^2_{-450}, respectively) are calculated, and the variance ratios $q^2_{-850} = \sigma^2_{\rm raw}/\sigma^2_{-850}$ and $q^2_{-450} = \sigma^2_{\rm raw}/\sigma^2_{-450}$ are found[5]. Fig. 1 shows q^2 for a random sample of data for the two atmospheric subtraction techniques; it is worth noting a few characteristics of these plots.

The absence of points below $q^2 = 1$ suggests that subtracting the residual atmospheric via either method *never* increases the noise in the time stream, and therefore should always be implemented. This subtraction removes residual $1/f$ noise in each bolometer's time series left after double-differencing. Subtracting the scaled $450\,\mu$m average is never as effective as subtracting the $850\,\mu$m array average, however, it is not a drastically worse technique, as the average ratio q^2_{-850}/q^2_{-450} is about 0.9. Interestingly, there seems to be little correlation between the weather (as measured by $\tau_{850\,\mu\rm m}\times$ the airmass of the observation) and the improvement in variance.

Because it is critical that the analysis method preserve the large scale structure in the data, the $450\,\mu$m subtraction method is applied in our SZ effect pipeline. However, as using the $850\,\mu$m data is more efficient for removing atmospheric noise, this approach can be used when searching for point sources in the maps. Therefore a pipeline has been created which uses the $850\,\mu$m average subtraction method to reduce data for finding point sources in the maps (as we discuss in the next sub-section), while the $450\,\mu$m atmospheric subtraction method is applied to the data for the SZ fit.

[4] Here, one file consists of between 20 minutes and an hour's worth of data; the exact duration of these files is unimportant, as the central limit theorem applies for anything more than a few minutes of double–differenced SCUBA data ($\gtrsim 100$ samples).

[5] It is important to note that q^2 is the average variance of the bolometers' time series, not the variance of the average time series.

2.5 Point source removal

After atmospheric removal, the $850\,\mu$m data are binned into a sky map with a pixel size of 3×3 square arc seconds. Any pixel observed less than 20 times is removed from further analysis, as the noise in these can be highly non-Gaussian (Coppin et al. 2005). This procedure generally rejects less than 1 per cent of the pixels in a map, so it is not a very costly cut. In mosaicked fields involving multiple pointings, the data are simply co-added. Removing noisy bolometers, calibration and performing atmospheric removal before this binning ensures that the data in such mosaicked fields are treated on an equal basis. A standard deviation map is also made for each field; this provides an estimate of the error in each pixel. These two maps are convolved with a Gaussian point spread function (PSF), resulting in a flux map and an error map for each field. The flux map is divided by the error map to produce a signal to noise ratio (S/N) map, which are shown in Fig. 2. The source fluxes and their significance in these maps are the same as those one would find by fitting the JCMT's PSF to unconvolved maps. The maxima in the flux or S/N maps are the locations of possible point sources.

The method used to identify possible point sources in these fields consists of selecting those points in the S/N map above a given threshold. For short integration time maps, which we define to have total integration times $t_{\rm int} < 15$ ks as listed in Appendix A, this threshold is 4σ, while for long integration time maps $t_{\rm int} \geqslant 15$ ks, we have chosen the threshold to be 3σ. These limits are chosen because the short integration time fields have a much higher incidence of spurious sources at the 3σ level than would be expected based on the quoted noise levels. A Gaussian PSF of the same flux as the removed point source is then subtracted from the unconvolved map, and the χ^2 for the difference is calculated. This statistic provides a measure of how similar the point source is to the telescope's fiducial beam; the area around a peak in the map poorly fit by the telescope's PSF is likely due to random fluctuations, additional fainter sources, or systematic noise effects, rather than a real source.

In some cluster fields significant point source detections occur where the SZ signal is expected to be strongest, within about 30 arcsec of the measured X-ray centre (these sources are noted in Appendix B). As naively subtracting flux from this region would erroneously decrease the measured SZ effect increment, we do not subtract these central sources from the time series. This can be justified by considering the characteristics of the sources of sub-mm emission in these cluster fields.

Gravitational lensing is known to magnify background sub-mm sources in many cluster fields. Lensing models de-magnify sources in the interior of the Einstein ring, even when relatively complex mass distributions are considered. Sub-mm sources behind the cluster would either be lensed to the Einstein ring and beyond, or be much dimmer than their unlensed brightness, thus leaving the central area of a cluster free from lensed emission. This type of source would only be problematic in low mass clusters, where the Einstein ring is close to the centre of the cluster. Fortunately, the SCUBA catalogue almost uniformly contains massive, rich clusters, so we expect little contamination from these sources.

The possibility of dust emission from the central galaxy is more problematic. As no measurements of pure dust emission in the far-infrared (FIR) in mid- to high-redshift cD galaxies exist, it is difficult to estimate the flux contribution expected from these sources. Vlahakis et al. (2005) show that early-type galaxies of a given mass are dimmer than comparable late-type galaxies, and since even canonical Ultraluminous Infrared Galaxies (ULIRGs)

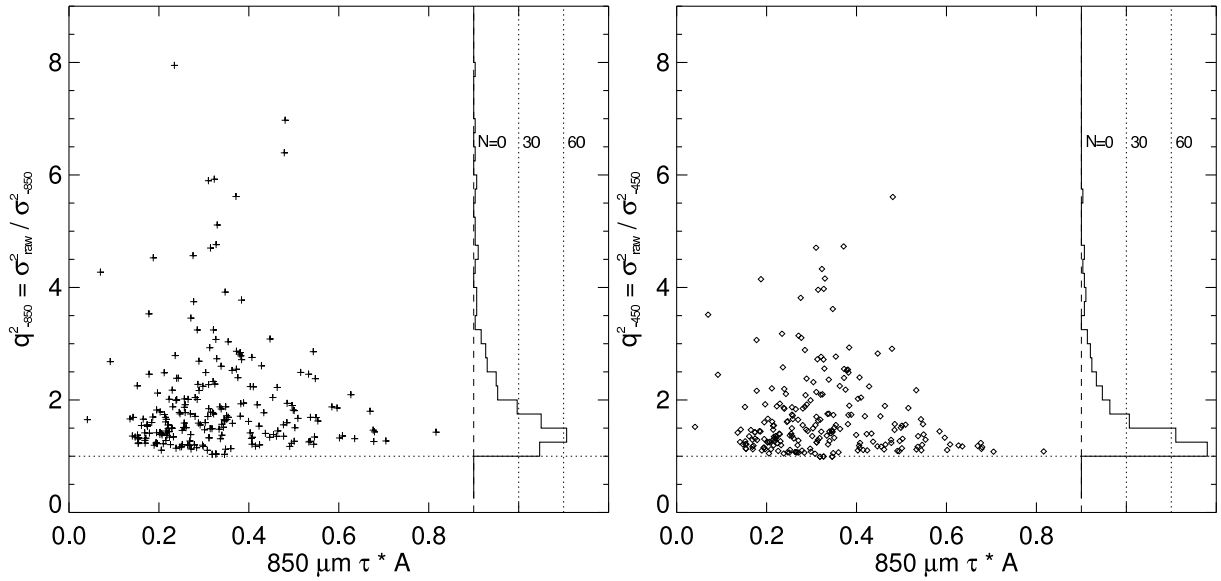

Figure 1. These plots compare the atmospheric removal methods. The left panel shows q^2_{-850} as a function of weather, as traced by $A \times \tau_{850}$ (where A is the airmass of the observation) for a random sample of 250 data files in our set. The right panel shows the quantity a^2_{-450} versus $A \times \tau_{850}$ for the same random sample. The histograms to the right of either of these plots show the distribution of both q^2. The ratios q^2 are always greater than 1, implying that some form of atmospheric removal should always be instituted. However, improvement from the $450\,\mu$m atmospheric removal method is systematically lower than for the standard $850\,\mu$m method. The average of the ratio q^2_{-850}/q^2_{-450} is about 0.9, meaning that the difference between the improvements for the two methods is not substantial. The overall improvement in variance after atmospheric removal is typically about a factor of 2; we find that generally, removing an array average does not improve an individual bolometer's noise performance by a large factor. However, some sort of array average subtraction is critical for the noise characteristic of the time series, as it removes residual $1/f$ noise left after double–differencing.

have fluxes less than 1 mJy at $z = 0.5$, a priori we expect little contamination from typical central cluster galaxies.

Should they in fact be sub-mm bright, there are two methods which could be used to identify central galaxies in these clusters. The first relies on the fact that, if present, such sources would be very bright at $450\,\mu$m. It is therefore necessary to check the $450\,\mu$m maps for sources coincident at both SCUBA frequencies; these would indicate that the central flux is indeed due to bright dust emission in the cluster's central galaxy. For example, consider the case of a $z = 0.5$ $850\,\mu$m central source with flux 5 mJy, similar to the situation in Cl 0016+16. A conservative estimate for the $450\,\mu$m flux of such a source based on dust emission alone is ~ 40 mJy, which would be detected in the $450\,\mu$m maps. Furthermore, in the class of clusters with detected central $850\,\mu$m emission, Cl 0016+16 has the second highest redshift, meaning that the $450\,\mu$m flux of central sources in the other cluster fields would be much stronger still[6]. The second method of identifying central cluster sources involves measuring the shape of the source in the map. A number of the central sources in these clusters appear to exhibit extended structure poorly fitting the telescope's PSF. Such sources (as in Abell 370, Abell 383, Abell 520, Abell 1689, and RXJ1347−1145) are unlikely to be galactic, as these should be unresolved.

This being said, a counter–example to the generalization that moderate redshift cD galaxies are sub-mm dim is the central galaxy detected in the $z = 0.25$ cluster Abell 1835, which multi-wavelength studies have shown to be an FIR bright cD galaxy (Edge et al. 1999). The image of this source in the SCUBA map shows it to be a point source well matched by the JCMT's PSF rather than extended emission, so even in the absence of measurements at other wavelengths it would be considered suspicious. This source is the only sub-mm bright cD galaxy identified in the literature and detected in our sample, and we argue that it is an exceptional example. In any case, this field is flagged as contaminated for the purposes of SZ effect measurement with these data.

It is certain that central cluster galaxies emit at $850\,\mu$m at *some* level; if the average brightness of these galaxies is ~ 1 mJy, which is much brighter than we would naively predict, they would be a significant contaminant for measurements of the SZ effect (this issue is discussed further in Sections 3.3 and 4). The sub-mm flux distribution of cluster sources is certainly an open topic, and one which merits further study.

Table 5 in Appendix B lists the point source candidates, positions, fluxes and their errors, and the χ^2 statistics for the binned maps. As none of the unresolved sources exhibit a poor spatial χ^2 statistic, they all meet our criteria for being real. For the purpose of measuring the SZ effect signature, all detected point sources must be removed from the data. We do this by subtracting all of the sources in Table 5 directly from the time series by sampling their idealized shape (i.e. the PSF shape with the same amplitude as the source's brightness) and subtracting the resulting time series from the real data. These cleaned data are used in subsequent stages of the analysis. Appendix C provides notes about each of these clusters, including references to previous SCUBA measurements of these fields.

In order to provide a check for the point source identification, the $450\,\mu$m data are also reduced using the SURF pipeline. The estimated $450\,\mu$m fluxes at the positions of the $850\,\mu$m sources are also listed in Appendix B. Only one $850\,\mu$m source is robustly detected at $450\,\mu$m, RXJ 1347−1145-1.

[6] The highest redshift cluster with a centrally–detected source, Cl1604+4304, is a poor choice for SZ effect measurements using the methods described in this work, as discussed in Section 3.2.1.

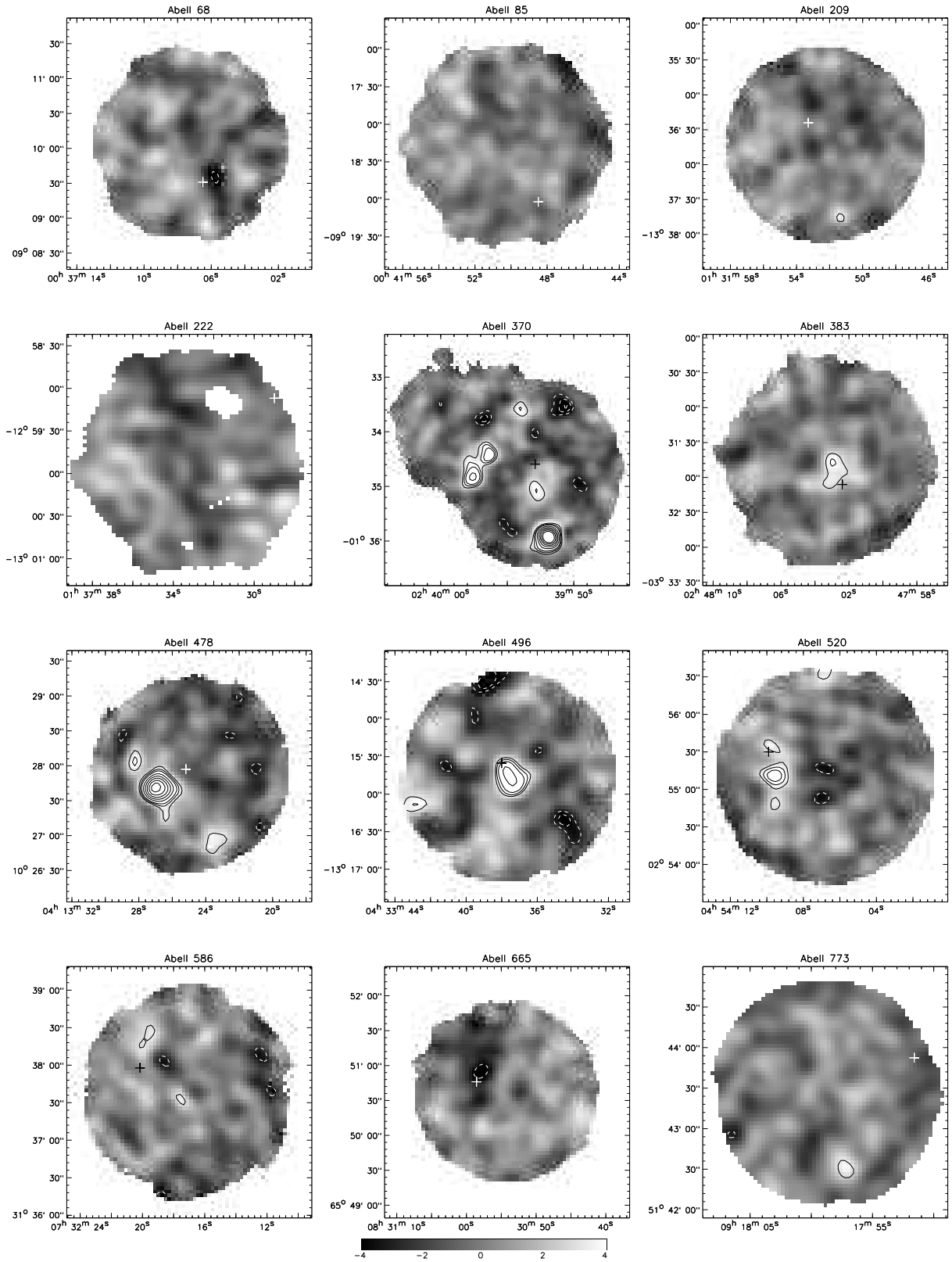

Figure 2. $850\,\mu$m signal to noise ratio maps of clusters in the SCUBA archive. The signal to noise ratio is used because the noise characteristics of these maps can be quite heterogeneous. Note that these images are useful for assessing the quality of the data and the contamination by bright sources, but do *not* show the entire SZ effect (since a large part of the signal comes from differences relative to the off-beams). The cross symbol shows the centre of the cluster as defined by X-ray data. For the long integration time fields ($t_{\rm int} \geqslant 15\,$ks), the dashed contours are at $\{-7, -5, -4, -3\} \times \sigma$ and the solid contours are at $\{3, 4, 5, 7, 9, 11, 13\} \times \sigma$, while for the short integration time fields ($t_{\rm int} < 15\,$ks), the dashed contours are at $\{-7, -5, -4\} \times \sigma$ and the solid contours are at $\{4, 5, 7, 9, 11, 13\} \times \sigma$. 'Holes' in the maps occur due to noisy bolometer subtraction, and generally occur only in fields with short integration times. Negative beams of sources can be seen in some of the maps where 'in-field' chopping was used. Abell 370 exhibits a bright source near the southern edge of the field, Abell 478 exhibits a bright quasar near the middle of the field, and Abell 496 shows emission associated with its central galaxy.

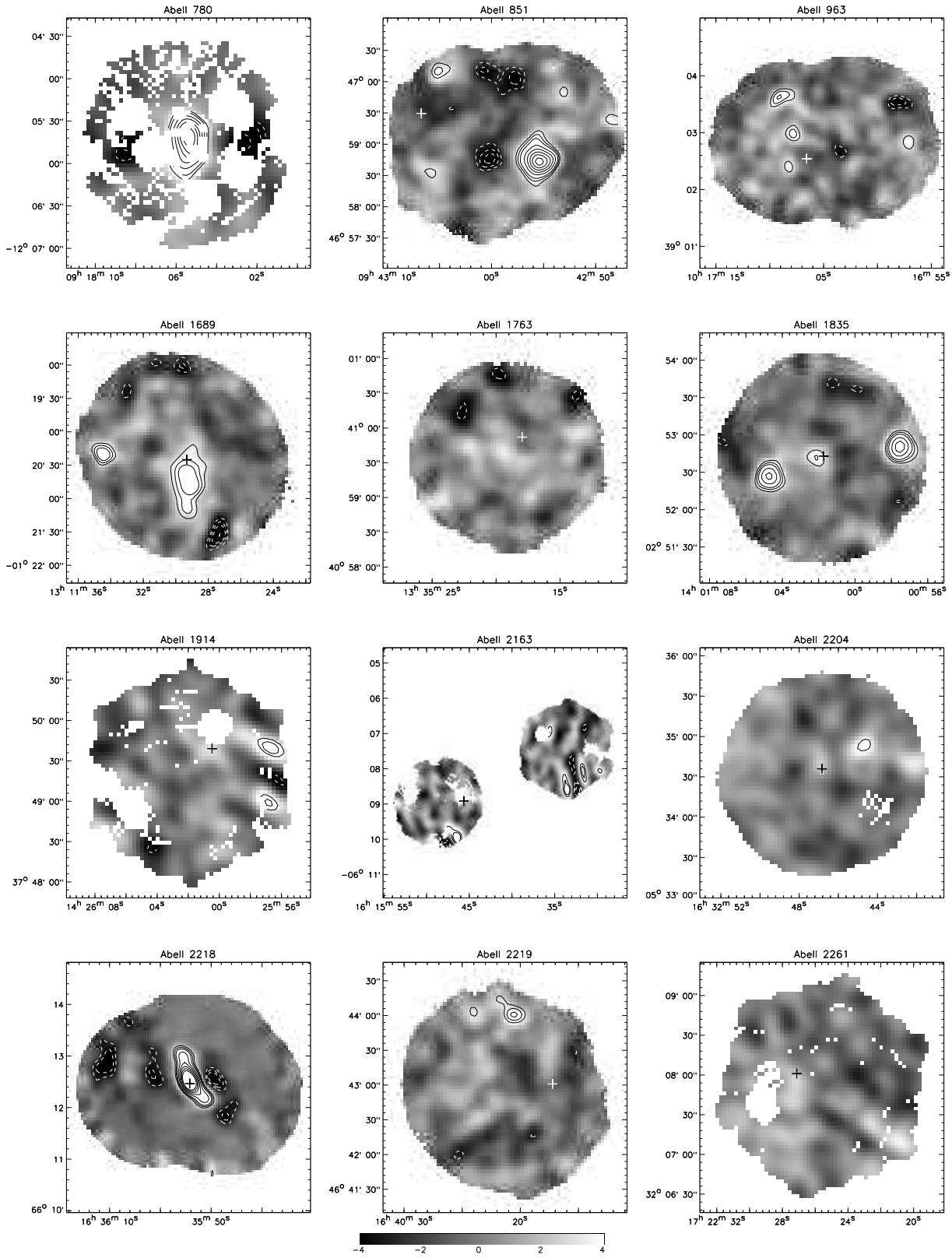

Figure 2 – *continued* Abell 780 contains the bright source Hydra A, which is visible in this image, which, due to short integration time is sparsely sampled. Abell 1689 contains an extended source near the X-ray centre; we associate this with the SZ effect (see Section 4). Abell 1835 also shows a significant detection at its centre, although this is associated with abnormally bright dust emission in the central cluster galaxy. Abell 2163 has two pointings, neither of which are very deep, and both of which show pathologies in the data; the cluster is removed from further analysis because of this. Abell 2218 contains a multiply imaged high redshift source (Kneib et al. 2004b); since this would interfere with SZ effect extraction, this cluster is also removed from further analysis (because the central source in this cluster is very significant, the contours in the Abell 2218 map are drawn at $(-5, -4, -3, 3, 6, 9, 12, 15, 18, 21) \times \sigma$).

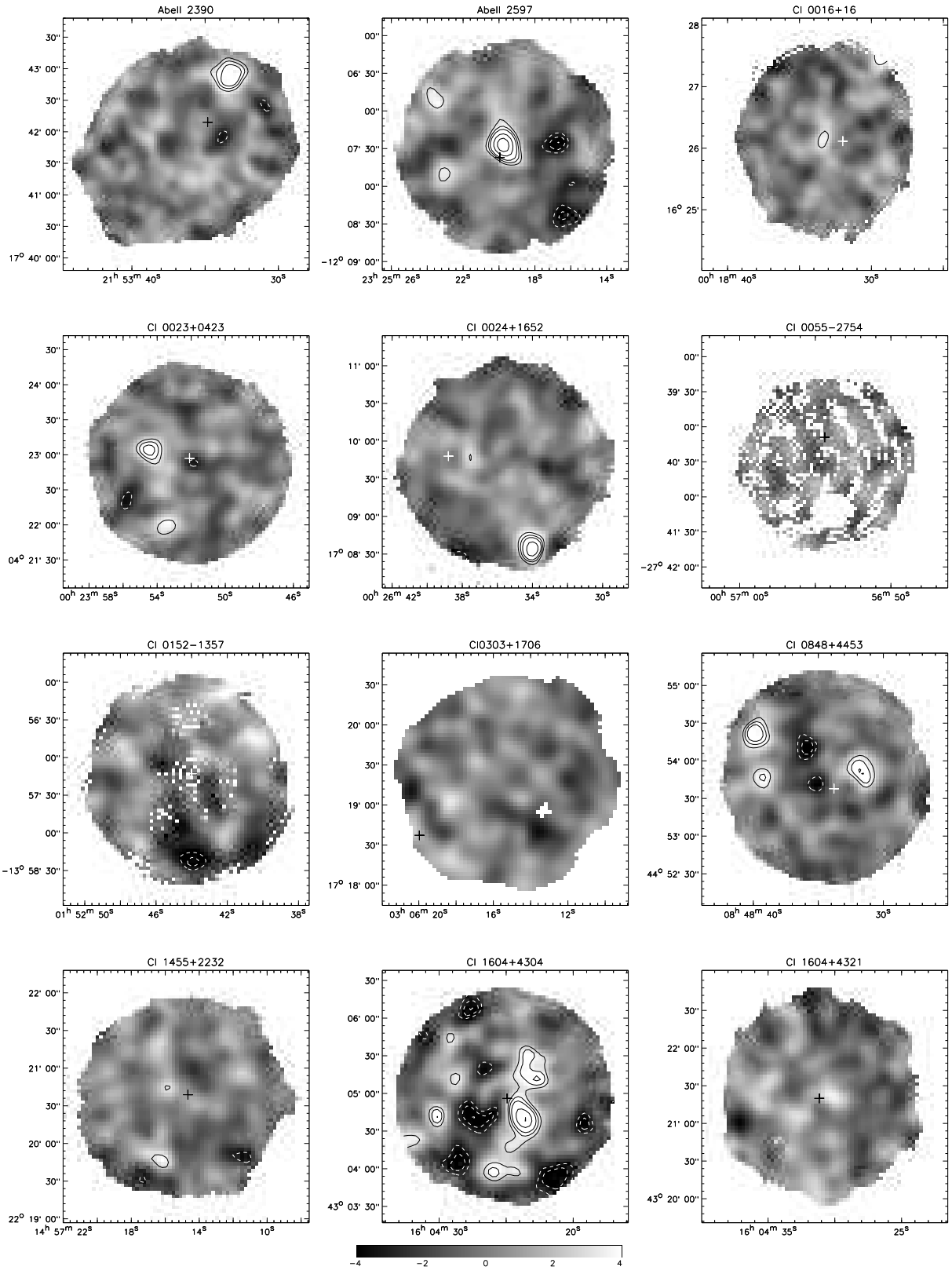

Figure 2 – *continued* Abell 2597 contains a bright point source associated with AGN activity in its central galaxy. Cl 0016+16 has a central enhancement which we ascribe to the SZ effect Zemcov et al. (2003). Cl 0055−2754 has a very short integration time and so is sparsely sampled. Cl 1604+4304, a high redshift cluster, appears to contains a large number of sources.

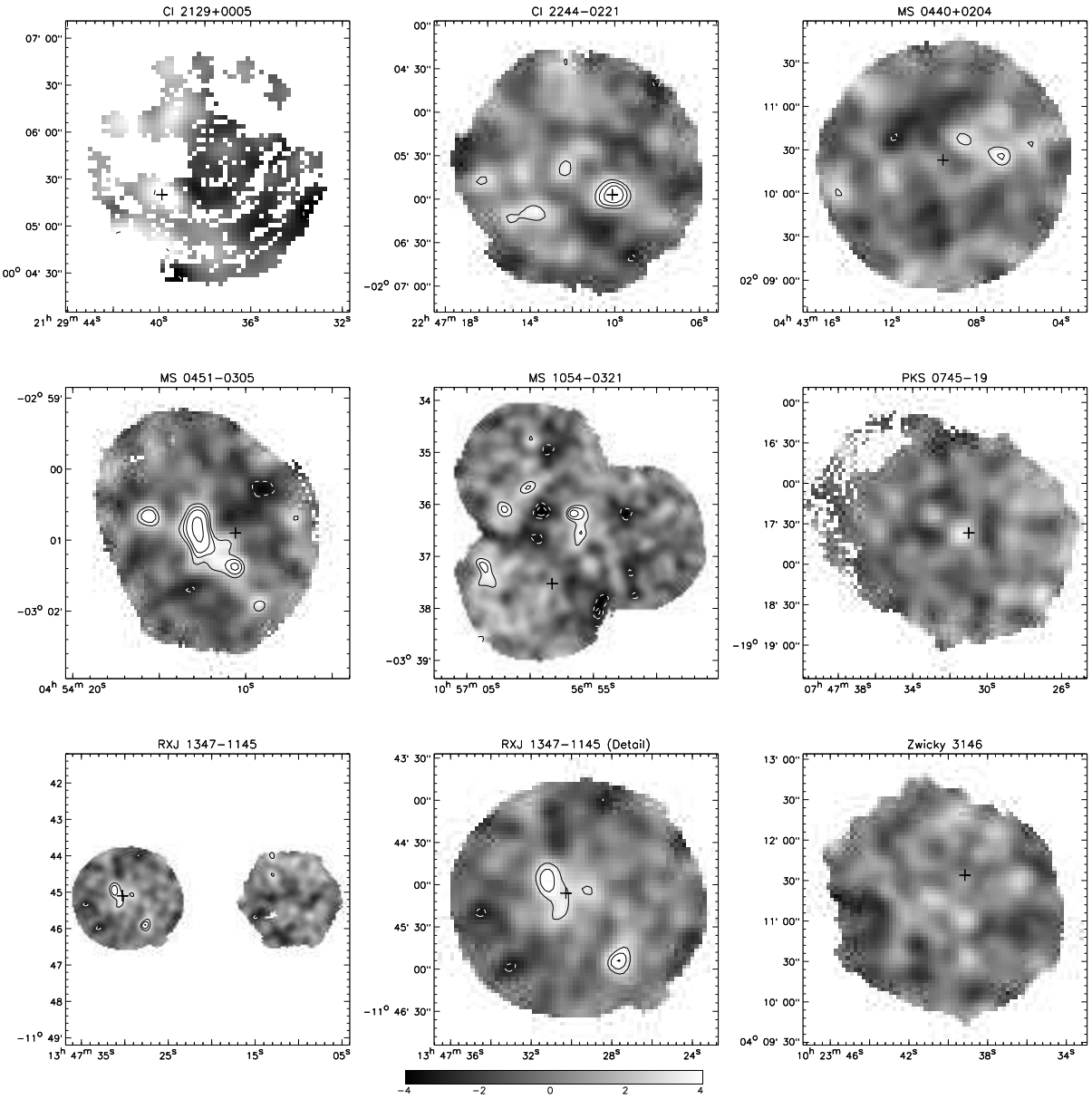

Figure 2 – *continued* Cl 2129+0005 is another field with an extremely short integration time. MS 0451−0305 contains another resolved gravitationally lensed source (or set of sources) at high redshift (Borys et al. 2004). Because the map of RXJ 1347−1145 covers such a large area, it appears twice; the lowest left map is the whole field, and the lowest middle map is a detail of the centre of the cluster. The central area of RXJ 1347−1145 contains a source bright at both 850 and 450 μm, and, potentially, a resolved image of the SZ effect in the centre of the cluster.

3 SZ INCREMENT FITTING

3.1 Field cuts

Although all of these clusters should exhibit the SZ effect, the signal from some may be swamped by known sub-mm bright central galaxies, complex emission due to gravitational lensing, and instrumental pathologies. Therefore we cull the list to exclude those fields where SZ emission at the ~ 1 mJy beam^{-1} level cannot possibly be disentangled from other sources of emission based on our present knowledge of the cluster.

We remove those clusters lying at low redshift ($z < 0.1$) with bright AGN near their centre which would swamp the SZ effect. The clusters affected by this cut are Abell 478, Abell 496, Abell 2597, Abell 780, and Cl 2129+0005. In general, these clusters were only observed for a short time, and have poor spatial coverage. Similarly, Abell 1835 is removed from the sample as it contains an abnormally bright cD galaxy coincident with the X-ray centre, as discussed in the last section.

A further cut removes two clusters with strong lensing signatures: Abell 2218 (Kneib et al. 2004b) and MS 0451−0305 (Borys et al. 2004). In these systems, it is too difficult to disentangle the complex lensed structure from the SZ effect. Abell 1835 is also cut from the sample, as it is known to harbour a sub-mm bright central source (Edge et al. 1999).

The two clusters (Cl 0055−2754 and Cl 2129+0005) with under 30 minutes of integration time are removed from further consideration; the noise level achievable in this time under even the best conditions is too high to see a $\sim$ 1 mJy beam^{-1} SZ effect.

Furthermore, neither X-ray data nor velocity dispersions are currently available, so we cannot apply our SZ fitting method to these clusters (as discussed in Section3.2).

The noise structure in the map of Abell 2163 is atypical, demonstrating elongated patches and deep negative holes. Despite our extensive background with SCUBA data, we are not able to explain this noise pathology, and therefore flag this cluster map as suspect and remove it from our sample.

After these cuts are applied, our initial SZ effect sample consists of 33 galaxy clusters. Using the version of the SCUBA time series and maps with point-sources removed, we now fit these data for the SZ increment.

3.2 Sunyaev–Zel'dovich effect modeling & fit

The isothermal β model is commonly used to parameterize the spatial distribution of the SZ effect, as discussed in, for example, Birkinshaw (1999). If θ is the angular distance from the centre of the cluster, $I(\theta)$ is the SZ effect intensity at θ, I_0 is the central SZ effect intensity, and β and $\theta_{\rm c}$ are values parameterizing the cluster, then the isothermal β profile is given by

$$I(\theta) = I_0 \left(1 + \frac{\theta^2}{\theta_{\rm c}^2}\right)^{(1-3\beta)/2}. \quad (3)$$

Given the low signal to noise ratio of our SCUBA data, we cannot hope to determine all of these parameters from our data alone. Fortunately there is a rich body of ancillary data that can be used to assist in the fits.

3.2.1 Independent measures of $\theta_{\rm c}$ and β

28 of 33 clusters in our sample have published X-ray and/or SZ decrement measurements from which $\theta_{\rm c}$ and β have been determined. These parameters and references are listed in Table 1.

Of the remaining 5 clusters, two (Abell 222 and Abell 851) have archival X-ray data[7] which we use to fit the center coordinates, $\theta_{\rm c}$, and β ourselves. To ensure our fitting procedure was robust, we downloaded and fit the model to archival data for clusters with already published $\theta_{\rm c}$ and β values, and found no significant discrepancies.

For the three remaining clusters for which we could find no archival X-ray data (Cl 0303+1706, Cl 1604+4304 and Cl 1604+4321), we assume the clusters are isothermal and have a standard King profile (i.e. $\beta = 2/3$). An estimate of the core radius $r_{\rm c}$ (which is related to $\theta_{\rm c}$ by the angular diameter distance) can be obtained via the line of sight velocity dispersion of the cluster $\sigma_{\rm r}$ (Sarazin 1988):

$$r_{\rm c}^2 = \frac{9\sigma_{\rm r}^2}{4\pi G \rho_0}. \quad (4)$$

Here a value for ρ_0 must be adopted, since no direct measurements of the central density of these clusters exist. If we estimate $n_{e0} = 10^{-2}\,{\rm cm}^{-3}$ and assume that globally the intra-cluster plasma is electrically neutral, then

$$\rho_0 \simeq n_{e0}(m_e + m_p), \quad (5)$$

where m_e and m_p are the electron and proton masses, respectively. This calculation yields the core radius estimates listed in Table 1.

[7] Reduced maps from NASA's High Energy Astrophysics Science Archive Research Centre were obtained.

A position must also be adopted for the X-ray and SZ peak. For Cl 1604+4304 and Cl 1640+4321, we assume that the optical centre as given in Gunn, Hoessel & Oke (1986) corresponds to the X-ray peak[8]. For Cl 0303+1706, Ueda et al. (2001) give an X-ray centre which we adopt. The model parameter predictions for these 3 clusters are listed in Table 1.

3.2.2 Fitting for the SZ increment

With these parameters in hand, we can fit for the amplitude of the SZ increment in the clusters, for which two different approaches have been adopted.

In the first method, a model map is made for each cluster using its isothermal β profile parameters. This map is convolved with the JCMT PSF and normalized to have a maximum of $1.0\,{\rm mJy\ beam}^{-1}$; this ensures that the fit discussed below yields a consistently calibrated result. This model map is then differenced in the same way as in the SCUBA observation, making a model time series. The mean of the model for each subset of data is removed to match the subtraction of the $\overline{R^{850}}$ from Equation 2 in the real data. The data are then fit to the model differences to determine a scaling coefficient which gives the central increment value. Because it directly incorporates our differencing scheme, this fit method obviates the need to track the correlations which would occur in a pixelization scheme.

The second method for determining the SZ effect amplitude involves making a map using the $S_{\rm b}^{850}(t)$ and fitting the result to the model. In this method, a model map is made and normalized in the same way as discussed above. This map is then differenced according to the actual SCUBA observation to produce a time series. Again, the $\overline{R^{850}}$ is subtracted from the model time series. This model data is then rebinned into a map in the same way as for the real data. The data map is then fit to the rebinned model time series to yield a scaling, which is the SZ effect amplitude for each cluster. This method allows a check on the robustness of time series analysis in each cluster.

The results of both methods are listed in Table 2, and are plotted against one another in Figure 3. Although there is some scatter between the methods, they generally agree, showing that the fitted SZ effect amplitude from these data is largely independent of the fit. However, the error bars from the map fit method are often $\sim 5\,\%$ larger than from the time series fit, and so we adopt the SZ effect amplitudes given by the first method as the best fitting increment values.

As a test of the assumptions about the effects of central point sources discussed in Section 2.5, these fits are also performed with the central 18 arcsec masked from the fit. This test allows a study of how strongly the fits depend on the data from the very central region of the cluster; an indication that point source contamination may be present is if the average fit amplitude is reduced in those clusters with central sources (the starred entries in Table 5). Since data are being removed from each set, the error bars should also increase.

To quantify the change in the fit amplitudes, the ratio of the un-masked to masked fit amplitude in each cluster is used; this should be unity for no change in the fit amplitude. For the entire sample listed in Table 2, the mean ratio is 1.003 and the standard

[8] While some archival *XMM-Newton* data exist for the supercluster field containing these two clusters, the data are not sufficiently deep to reliably extract model parameters.

Table 1. Summary of the isothermal β model parameters in the SZ sample. The first part of the table lists the parameters for clusters with good model parameters and X-ray centres in the literature. The second part of the table lists model parameters and centres derived from archival X-ray data. The third part of the table lists the assumed parameters for clusters with no available X-ray data (how these parameters are dervied is discussed in Section 3.2).

Cluster	z[a]	α_{2000} (hh:mm:ss)	δ_{2000} (+dd:mm:ss)	$\theta_{\rm c}$ (arcsec)	β	$T_{\rm e}$ (keV)	Refs.[b]
Cluster parameters available in the literature.							
Abell 68	0.255	00:37:06.7	+09:09:28	55.1	0.764	9.5	1, 18, 18
Abell 85	0.052	00:41:48.7	−09:19:05	122.4	0.6	4.8	19, 19, 29
Abell 209	0.206	01:31:53.5	−13:36:27	36.5	0.50	8.5	6, 27, 6
Abell 370	0.374	02:39:53.2	−01:34:40	61.8	0.811	6.6	14, 18, 22
Abell 383	0.187	02:48:02.6	−03:32:09	9.4	0.51	7.5	6, 27, 6
Abell 520	0.202	04:54:10.3	+02:55:24	123.3	0.844	8.3	3, 25, 2
Abell 586	0.171	07:32:20.4	+31:37:55	45.3	0.723	7.2	3, 18, 3
Abell 665	0.182	08:30:59.1	+65:50:43	17.7	0.454	9.3	25, 18, 2
Abell 773	0.217	09:17:52.1	+51:43:48	38.7	0.594	9.3	8, 18, 2
Abell 963	0.206	10:17:07.0	+39:02:28	22.6	0.51	6.1	7, 27, 2
Abell 1689	0.183	13:11:29.5	−01:20:28	48.4	0.688	13.2	9, 18, 33
Abell 1763	0.223	13:35:18.2	+40:59:49	42.0	0.6	6.9	5, 24, 24
Abell 1914	0.171	14:26:00.8	+37:49:36	44.0	0.734	10.9	26, 18, 13
Abell 2204	0.152	16:32:47.0	+05:34:33	33.7	0.614	7.4	3, 18, 3
Abell 2219	0.228	16:40:17.5	+46:42:58	103.8	0.79	12.4	9, 9, 3
Abell 2261	0.224	17:22:27.3	+32:07:58	28.9	0.624	8.8	3, 18, 3
Abell 2390	0.228	21:53:35.1	+17:42:06	51.9	0.67	10.1	9, 9, 3
Cl 0016+16	0.544	00:18:32.2	+16:26:04	42.8	0.742	7.6	17, 18, 16
Cl 0024+1652	0.39	00:26:39.0	+17:09:45	10.4	0.475	4.5	30, 30, 23
Cl 0152−1357	0.833	01:52:44.2	−13:57:16	32.7	0.73	5.5	20, 20, 20
Cl 0848+4453	1.261	08:48:34.2	+44:53:35	14.3	0.85	3.2	28, 31, 10
Cl 1455+2232	0.258	14:57:15.0	+22:20:36	11.2	0.643	4.8	3, 21, 3
Cl 2244−0221	0.328	22:47:10.4	−02:06:00	224	0.666	6.5	1, 22, 22
MS 0440+0204	0.197	04:43:09.8	+02:10:20	9.1	0.521	5.5	12, 21, 24
MS 1054−03	0.823	10:56:58.6	−03:37:36	57.7	0.884	7.8	11, 18, 31
PKS 0645−19	0.103	07:47:31.3	−19:17:40	19.0	0.48	6.7	15, 15, 2
RXJ 1347−1145	0.451	13:47:30.6	−11:45:09	17.7	0.651	12.2	4, 18, 4
Zwicky 3146	0.291	10:23:39.3	+04:11:31	30.4	0.736	6.4	9, 18, 3
Cluster parameters derived from archival X-ray data (columns as above).							
Abell 222	0.214	01:37:29.2	−12:59:10	98	0.42	*ASCA*	
Abell 851	0.407	09:43:07.2	+46:59:25	60	0.47	*XMM-Newton*	
Cluster parameters derived from velocity dispersions[c] *(columns 1–4 as above).*							
				$\sigma_{\rm r}$ km s^{-1}	$\theta_{\rm c}$ arcsec		Refs.[d]
Cl 0303+1706	0.420	03:06:20.3	+17:18:22	876	46		1, 1
Cl 1604+4304	0.895	16:04:25.2	+43:04:53	1226	46		2, 3
Cl 1604+4321	0.92	16:04:31.5	+43:21:17	935	35		2, 3

[a] as listed in the NASA/IPAC Extragalactic Database, `http://nedwww.ipac.caltech.edu/`
[b] In order, references are given for the central X-ray/SZ effect position, isothermal β model parameters and X-ray temperature: (1) This work; (2) Allen & Fabian (1998); (3) Allen (2000); (4) Allen, Schmidt & Fabian (2002); (5) Böhringer et al. (2000); (6) Cruddace et al. (2002); (7) David, Forman & Jones (1999); (8) Ebeling et al. (1998); (9) Ettori & Fabian (1999); (10) Ettori et al. (2004); (11) Gioia & Luppino (1994); (12) Gioia et al. (1998); (13) Govoni et al. (2004); (14) Grego et al. (2000); (15) Hicks et al. (2002); (16) Hughes & Birkinshaw (1998); (17) LaRoque et al. (2003); (18) LaRoque et al. (2006); (19) Mason & Myers (2000); (20) Maughan et al. (2003); (21) Mohr et al. (2000); (22) Ota et al. (1998); (23) Ota et al. (2004); (24) Ota & Mitsuda (2004); (25) Reese et al. (2002); (26) Reiprich & Böhringer (2002); (27) Rizza et al. (1998); (28) Rosati et al. (1999); (29) Sanders, Fabian & Allen (2000); (30) Soucail et al. (2000); (31) Vikhlinin et al. (2002); and (32) Xue & Wu (2002).
[c] This assumes the standard King profile, $\beta = 2/3$; see text for details.
[d] References for the coordinates and velocity dispersions for these clusters are given in: (1) Ueda et al. (2001); (2) Gunn, Hoessel & Oke (1986); and (3) Postman et al. (2001).

Table 2. Summary of fits for the full sample of SZ effect clusters.

Cluster	Fit to time series differences			Fit to maps		
	$\Delta I_0^{\rm D}$ (mJy beam^{-1})	$\sigma_{\Delta I_0}$	χ^2 / dof	$\Delta I_0^{\rm D}$ (mJy beam^{-1})	$\sigma_{\Delta I_0}$	χ^2 / dof
Cluster parameters available in the literature.						
Abell 68	-0.82	6.97	216811 / 216863	-5.94	7.71	2595 / 2574
Abell 85	-9.00	5.28	185611 / 185608	-11.6	5.91	2344 / 2503
Abell 209	1.23	5.22	418709 / 418714	-1.62	5.95	2628 / 2698
Abell 370	1.23	0.50	2310458 / 2309321	1.36	0.72	5030 / 4962
Abell 383	2.41	1.10	609370 / 609435	5.31	1.70	2873 / 3061
Abell 520	4.07	0.89	1046636 / 1046535	4.28	1.17	3046 / 2862
Abell 586	3.03	0.72	347668 / 347635	3.08	0.90	2812 / 2635
Abell 665	-16.6	5.1	131713 / 131737	-22.4	5.4	2346 / 2325
Abell 773	-4.60	4.08	390417 / 390424	-5.58	4.4	2618 / 2652
Abell 963	-0.48	0.90	1435408 / 1435505	-0.13	1.26	4351 / 4195
Abell 1689	4.57	0.60	1380185 / 1380135	5.81	0.81	3386 / 3295
Abell 1763	4.44	4.07	241500 / 241486	5.07	4.34	2628 / 2578
Abell 1914	5.09	1.56	62040 / 62031	5.80	1.68	2322 / 1880
Abell 2204	-1.46	2.17	83979 / 83974	-3.16	2.25	2262 / 2167
Abell 2219	5.85	3.38	530006 / 529787	-5.71	4.35	2915 / 2996
Abell 2261	0.98	1.86	86203 / 86215	0.90	2.01	2199 / 2158
Abell 2390	3.88	0.71	1678464 / 1677409	1.99	1.55	3994 / 3728
Cl 0016+16	3.31	1.06	522576 / 522593	2.94	1.36	2978 / 3052
Cl 0024+1652	5.26	1.46	282693 / 282676	5.41	1.96	2610 / 2575
Cl 0152−1357	1.34	1.05	228807 / 228596	0.19	1.16	2490 / 2433
Cl 0848+4453	-0.19	0.58	486137 / 486050	-0.58	0.61	2751 / 2659
Cl 1455+2232	0.80	1.14	238292 / 238325	0.08	1.24	2492 / 2548
Cl 2244−0221	18.0	18.1	423645 / 423625	17.9	19.3	2899 / 2654
MS 0440+0204	0.17	0.77	668865 / 668959	0.84	1.09	2892 / 2829
MS 1054−03	0.95	0.68	2855763 / 2856074	-0.64	0.82	7457 / 7235
PKS 0645−19	-1.45	2.63	153568 / 153557	-2.30	2.97	2680 / 2778
RXJ 1347−1145	8.80	0.84	876116 / 876350	9.06	2.10	5212 / 5392
Zwicky 3146	1.47	1.01	208741 / 208776	1.81	1.16	2865 / 2807
Cluster parameters derived from archival X-ray data (columns as above).						
Abell 222	-24.6	8.0	158325 / 158329	-25.8	8.7	2462 / 2304
Abell 851	-10.1	2.5	1328111 / 1327919	-7.24	3.75	4088 / 4024
Cluster parameters derived from velocity dispersions (columns as above).						
Cl 0303+1706	5.66	6.29	220745 / 220752	2.79	6.15	2360 / 2482
Cl 1604+4304	4.53	0.91	714956 / 714771	4.34	0.95	3026 / 2795
Cl 1604+4321	2.51	1.31	242345 / 242337	3.09	1.36	2466 / 2453

deviation of the ratios is 0.22; this means that, on average, the fit is unchanged, although there is some scatter in the ratio on a cluster by cluster basis. The average ratio for clusters with detected central point sources is 0.995 ± 0.240; this is also consistent with no change, on average. In addition to these amplitude changes, the average error bar for the fits increases by 7 per cent, as expected.

Based on this analysis, we conclude that there is no significant difference between the fits for clusters with and without detected central point sources. Furthermore, this test suggests that the methods we employ are mostly sensitive to the shape of the SZ effect in the data, rather than the brightness of the centre–most region alone. In the absence of results supporting the proposal that these fits are strongly contaminated by central point sources, the fit results which include the central regions for each cluster are quoted hereafter.

3.3 Sunyaev-Zel'dovich effect limits

Because the typical SZ effect in these clusters is expected to be $\sim 1\,$mJy beam^{-1}, cluster fields with short integration times will have noise levels much greater than the expected signal, and merely increase the noise in the overall measurement. Because they provide relatively uninteresting estimates of ΔI_0, the cluster fields with low integration times ($t_{\rm int} < 15\,$ks as discussed in Section 2.5) are excluded from the results presented in this section. Also, clusters whose model parameters are derived from the cluster's velocity dispersions or poor X-ray data are suspect; although these *may* be a reasonable estimate of the model, the potential error in the model dominates the statistical error in the data. These clusters are also excluded from this section. These criteria leave a final SZ sample of 17 clusters, listed in Table 3.

At 450 μm, the SZ distortion is a small but non-zero fraction of its peak. Because the $450\,\mu$m array averages, which contain the differenced SZ effect flux, have been removed from the data as part of the atmospheric removal method, the fits to the isothermal β

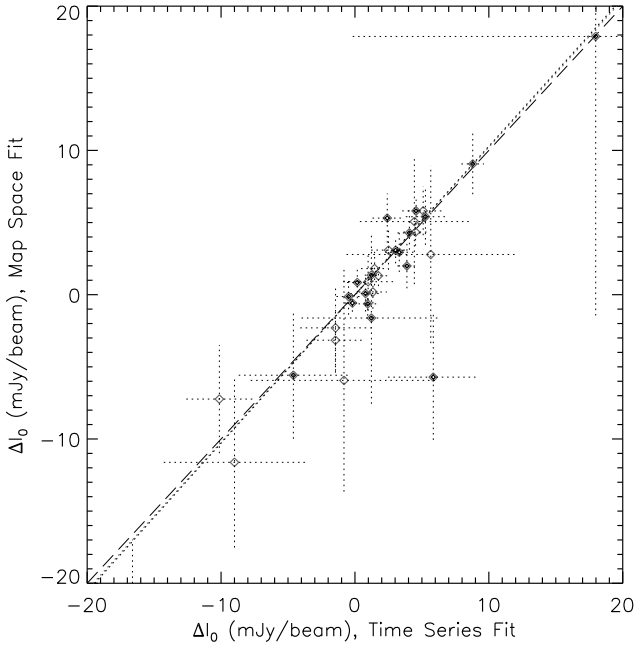

Figure 3. Comparison of fitting the SZ effect model to the time series data (shown on the abscissa axis) and the binned map data (shown on the ordinate axis). The points show the amplitudes from the fits, with their associated $1\,\sigma$ error bars. The points with dark centres highlight the 17 final SZ effect clusters defined in Section 3.3. The dark dashed line shows the line $x = y$, while the light dotted line shows the result of a linear fit to all 33 points, and the dark dotted line shows the result of a linear fit to the 17 final SZ cluster points. The fits have slopes very close to 1, and so are difficult to differentiate on this plot. This shows that the two methods yield very similar results in most of the clusters. The point near $\{-6, 6\}$ is for Abell 2219; it is unclear why it lies so far from the expected relation, although the application of a poor model is the most likely cause.

model must be corrected for the flux removed by this procedure (see Zemcov et al. 2003). The relation between the quantity measured by our isothermal β fits, $\Delta I_0^{\rm D}$, and the true peak SZ flux at $850\,\mu$m, ΔI_0^{850}, is given by

$$\Delta I_0^{850} = \Delta I_0^{\rm D} + \Delta I_{\rm ave}^{450}, \qquad (6)$$

where $\Delta I_{\rm ave}^{450}$ is the flux of the SZ effect removed by the subtraction of the scaled $450\,\mu$m array averages. To determine $\Delta I_{\rm ave}^{450}$, we adopt the procedure discussed in Zemcov et al. (2003). For each cluster, the SZ shape as defined by the isothermal β model is sampled in the same way as in the experiment, and a linear coefficient ξ relating the ratio of the input SZ amplitude to the mean of the sampled data stream is found. This gives $\Delta I_{\rm ave}^{450} = \xi \Delta I_0^{450}$, where ξ includes the gain difference between the $450\,\mu$m and $850\,\mu$m channels. The ξ coefficients are given in Table 3.

For each cluster, the best fit ΔI_0^{850} and error bar σ_{850} are found using a likelihood function and determining its maximum and associated 68 % confidence limits. The likelihood function is created by making a set of SZ effect models with different Compton y_0 parameters. At $850\,\mu$m, non-thermal corrections to the thermal SZ effect can change the best fitting amplitudes by as much as 15 per cent, given the temperatures of the clusters in the sample (although typically the corrections are much smaller, around a few per cent for most clusters). To account for this, the corrections to fifth order discussed in Itoh, Kohyama & Nozawa (1998) are applied to these fits, using the electron temperatures listed in Table 1. These temperatures are derived from averages over X-ray data for each cluster measured on angular scales similar to those measured with SCUBA; this reduces or eliminates the effect of biases associated with cooling flows in the central regions of the clusters. The difference $\Delta I_0^{850} - \xi \Delta I_0^{450}$ is found from this model. The difference which most closely matches the observed $\Delta I_0^{\rm D}$ yields the best fitting y_0. An integral under the likelihood function is used to determine the 68 % confidence limits, which are quoted as $1\,\sigma$ errors in the two values. The best fitting ΔI_0^{850} is converted from mJy beam^{-1} to MJy sr^{-1} by multiplying by the integral over the Gaussian JCMT PSF with FWHM 14.7 arcsec (equivalent to a conversion factor $1\,{\rm mJy\ beam^{-1}} = 5.739\,{\rm MJy\ sr^{-1}}$). The ΔI_0^{850}, y_0, and their associated errors for each of the final SZ clusters are quoted in Table 3. Also included in this table is the parameter $\mathcal{D} = I_{\rm ave}^{450}/I_0^{850}$, which is the ratio of the flux removed due to the use of the $450\,\mu$m channel as an atmospheric monitor to the total $850\,\mu$m SZ flux. This ratio is typically less than 5 per cent, but ranges between 0 and 15 per cent in this sample of clusters.

A common technique used in to draw a significant measurement from a set of noisy astronomical data is to 'stack' the noisy images on top of one another centred on a nominal source position. Using the SCUBA maps from the 17 deep integration fields, we have performed this procedure with these data. The (non-central) sources in these maps are subtracted out before the co-addition to give a clean signal from the SZ effect alone[9]. These individual maps are weighted using the expected central Compton parameter in each cluster, which is given by $y_0 \propto \sqrt{\Omega_{\rm M} + (1+z)^3 \Omega_\Lambda}\, T_{\rm e}^{3/2}$ (as discussed in, for example, Benson et al. 2004). Here we use the WMAP concordance cosmology (Spergel et al. 2006) and the cluster parameters listed in Table 1. In the cluster co-addition, each

Table 3. SZ effect parameters derived from archival SCUBA data. Listed are the cluster name, correction factor for the $450\,\mu$m atmosphere subtraction ξ, $\mathcal{D} = \Delta I_{\rm ave}^{450}/\Delta I_0^{850}$, and relativistic effect corrected amplitudes in both MJy sr^{-1} and (unitless) y_0.

Cluster	ξ	$\mathcal{D}$ $\times 10^2$	ΔI_0^{850} MJy sr^{-1}	y_0 $\times 10^4$
Abell 209	0.044	1.3	$0.22^{+0.80}_{-0.80}$	$1.38^{+5.02}_{-5.02}$
Abell 370	0.164	4.4	$0.22^{+0.09}_{-0.09}$	$1.38^{+0.56}_{-0.56}$
Abell 383	0.073	2.1	$0.43^{+0.19}_{-0.19}$	$2.66^{+1.20}_{-1.18}$
Abell 520	0.255	7.6	$0.77^{+0.17}_{-0.17}$	$4.82^{+1.06}_{-1.06}$
Abell 586	0.535	15.0	$0.62^{+0.15}_{-0.15}$	$3.86^{+0.94}_{-0.92}$
Abell 773	0.006	0.2	$-0.80^{+0.59}_{-0.59}$	$-5.12^{+3.74}_{-3.74}$
Abell 963	0.043	1.1	$-0.09^{+0.12}_{-0.12}$	$-0.52^{+0.74}_{-0.74}$
Abell 1689	0.277	10.4	$0.87^{+0.12}_{-0.12}$	$5.64^{+0.74}_{-0.74}$
Abell 2219	0.084	3.1	$1.05^{+0.57}_{-0.57}$	$7.02^{+3.76}_{-3.78}$
Abell 2390	0.149	4.8	$0.71^{+0.13}_{-0.13}$	$4.58^{+0.86}_{-0.84}$
Cl 0016+16	0.00	0.0	$0.58^{+0.19}_{-0.18}$	$3.60^{+1.16}_{-1.14}$
Cl 0024+1652	0.117	2.8	$0.94^{+0.26}_{-0.26}$	$5.60^{+1.56}_{-1.56}$
Cl 0848+4453	0.070	1.5	$-0.03^{+0.09}_{-0.09}$	$-0.20^{+0.52}_{-0.52}$
Cl 1455+2232	0.339	8.2	$0.15^{+0.15}_{-0.15}$	$0.90^{+0.92}_{-0.90}$
MS 0440+0204	0.142	3.6	$0.03^{+0.12}_{-0.12}$	$0.20^{+0.74}_{-0.74}$
MS 1054−03	0.018	0.5	$0.17^{+0.11}_{-0.11}$	$1.04^{+0.68}_{-0.68}$
RXJ 1347−1145	0.135	4.5	$1.59^{+0.16}_{-0.15}$	$9.82^{+0.96}_{-0.94}$

[9] If this subtraction is not performed, the co-added map shows both the central extended emission *and* a diffuse ring of emission with radius slightly larger than half an arc minute. This is good evidence that, statistically, dim gravitationally lensed sources tend to be re-imaged at or beyond the average Einstein ring in these clusters.

pixel is given a weight based on the variance map, and a total variance map is made using the same cosmological weight as above. The total number of hits in each pixel is also calculated, and this can be used to apodize the co-added maps if desired. The resulting signal map is shown in Figure 4.

The co-addition is quite successful at drawing out extended central structure in these maps. The peak increment value (even without adjusting for the SCUBA chop) is detected at 9σ based on the set of 17 deep maps. Comparison of this co-addition with a model map is desirable; this is achieved as follows. Using the model parameters given above, an isothermal β model is created for each cluster. This input model map is then convolved with the JCMT's PSF and differenced according to the real data. Time series averages are subtracted as in the SZ effect fitting pipeline, and a model SCUBA map is made using these model data for each cluster. These model chopped maps are then co-added using the real noise weights for each pixel in each cluster. The coadded maps for both the data and the model can then be averaged in radial bins to facilitate a comparison of the average flux as a function of radius, as is shown in Figure 5.

This comparison shows that the model and data stacked maps agree very well from about $0.3 \lesssim r \lesssim 3$ arcmin, where the data begin to sparsely sample the sky. However, the first bin (which has radius equal to a SCUBA beam) is approximately a factor of two, or about 0.75 mJy, higher than the SZ-only model would predict. This region is typically not resolved in prior SZ effect measurements, so these data provide new insight into models for SZ effect distributions. The excess emission is difficult to explain in the context of our current (isothermal β) model of these clusters, which includes only the SZ effect and sub-mm bright sources in the region away from a cluster's centre. The extra flux therefore could be the signature of unresolved point sources or complex ICM temperature distributions in these clusters. If this extra flux is wholly attributable to the central galaxy in the cluster, a measurement of 0.75 ± 0.25 mJy is obtained for the average flux of such sources over 17 clusters in the range $0.17 < z < 1.2$. It is difficult to consistently apply a more complex ICM model to these data, but some fraction of the extra flux may be attributable to varying temperature distributions or clumping in the cluster electron gas, as would occur in the presence of cooling flows, for example. As the isothermal β model relies on fairly simple physical assumptions (some of which are not true in a subset of these clusters), it is quite plausible that it fails as an accurate description of the true ICM shape in some fraction of the sample. However, any other model invoked to describe these data would need to provide a factor of 2 greater SZ emission inside the central ~ 100 kpc of each of these clusters, or an even larger factor in some subset of them. It is most likely that the excess emission is due to some combination of a more peaked model, at least in some subset of the clusters, and dim galactic sources near the clusters' centres.

4 DISCUSSION

4.1 Sunyaev–Zel'dovich effect results

From a rather heterogeneous data set, the methods employed here have allowed us to estimate the SZ effect brightness in archival SCUBA data for 17 galaxy clusters. For the other 27 clusters with archival SCUBA data, we were unable to provide strong constraints on the the SZ increment. This is due to a variety of factors, such as contamination from lensed sources behind the cluster, AGN in the cluster, and low on-source integration times. In general, the combination of chopping pattern, extended emission and noise means that images of the cluster fields within the size of the array do not fully represent the SZ signal. However, it appears as though our maps of several clusters (particularly Abell 370, Abell 1689, and RXJ $1347-1145$) *do* show significant emission at approximately the right brightness and shape to be (chop–filtered) images of the SZ effect.

A number of the clusters observed with SCUBA have also been popular SZ effect targets with other instruments (see Appendix C for a discussion of this). It is instructive to compare the results given here with those of other groups; we have searched the literature for other SZ effect measurements for each of these clusters and Fig. 6 shows the results.

Comparing to the other SZ effect measurements in these clusters shows that the SCUBA y_0 results presented in this work are substantially larger than those determined from data taken at SZ decrement frequencies in 5 of 8 clusters. Although there appears to be a correlation with the results of SuZIE II (Benson et al. 2004), which uses data from frequencies on both sides of the null of the SZ effect, this is difficult to quantify with the data at hand. The systematic preference for larger y_0 evident in the SCUBA measurements in comparison with measurements at other frequencies may be due to some poorly accounted for effect in the analysis or methodology; we discuss these here.

Given these results, a primary candidate for systematically increasing the measured SZ flux is point source contamination near the centre of the cluster fields. Even a relatively dim radio/mm point source near the centre of these clusters could serve to increase the y_0 measured from observations taken at SZ increment frequencies, and decrease the y_0 measured from SZ decrement observations. On average, such sources would thus increase the disagreement between measurements on either side of the SZ effect null. This being said, the results presented in Section 3.2.2 suggest that point source contamination, at least on average, is not a strong effect in these data. Similarly, experiments targeting the SZ decrement are typically careful to quantify the number and fluxes of point sources in their target fields (e.g. Cooray et al. 1998). On the other hand, the excess emission found in the average of 17 cluster maps discussed in Section 3.3 suggests that as much as 0.75 mJy of the central flux cannot be explained by the isothermal β model alone. This is roughly the same size as the expected SZ effect in these clusters; we would therefore expect an appreciable bias to affect the fits due to central point sources below the detection threshold[10]. It is not clear whether the excess flux is in fact due to point sources, however.

A second important concern is the model assumed in each cluster. The isothermal β model, while an accurate description of the ICM flux distribution in some clusters, fails badly in others. For example, Benson et al. (2004) show that the assumed model can have a large effect on the y_0 amplitudes measured in their cluster set. To attempt to quantify the dependence of our fitted amplitudes on the model, the model parameters are varied and the data are reanalyzed. We find that the fitted SZ increment amplitudes are a weak function of θ_c: a systematic increase of a factor of 2 in θ_c for all of the clusters listed in Table 2 leads to an increase in the fitted ΔI_0 of 15 ± 4 per cent (the quoted error bar reflects the standard

[10] Although not a factor of two, as increasing the value of a single pixel in the flux distribution does not have a large effect on the best fitting value; this is not true of the χ^2 of the fit, however.

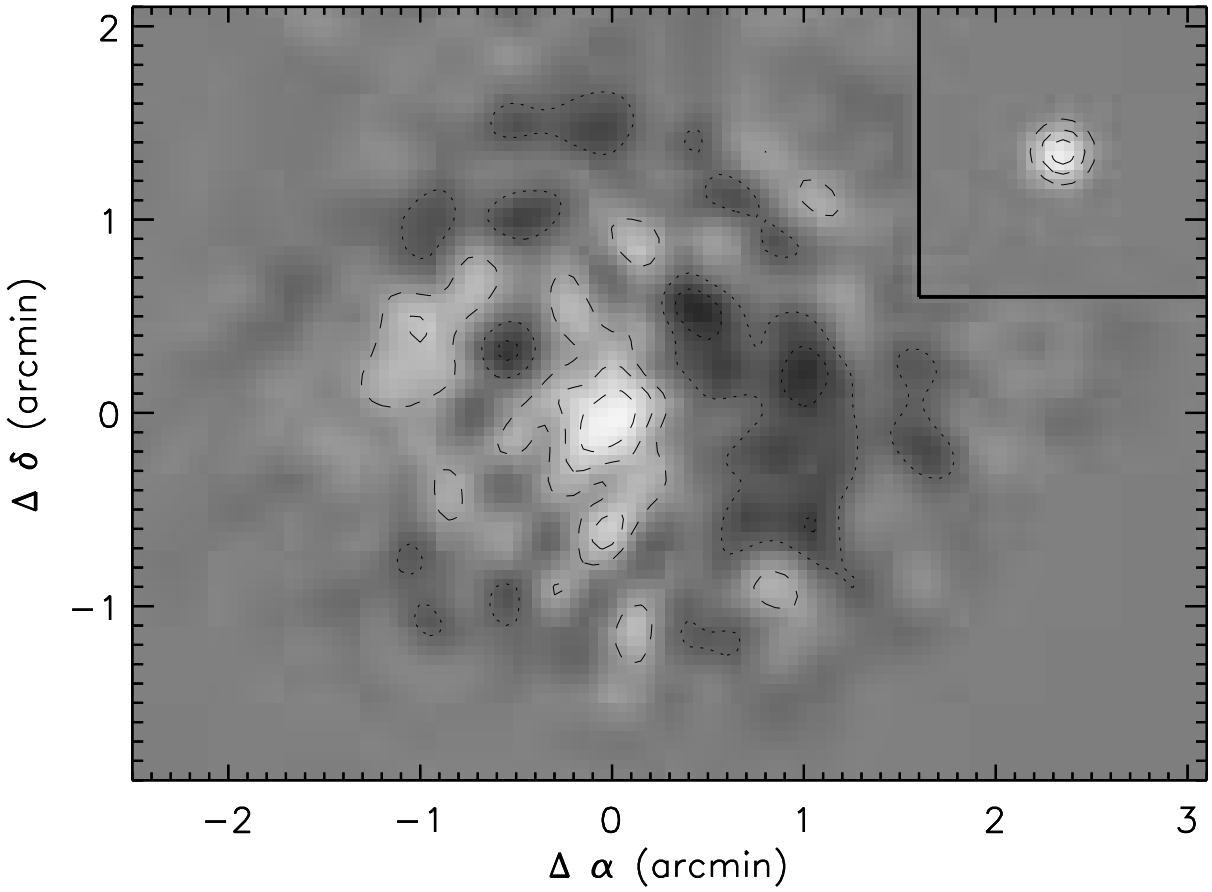

Figure 4. This figure shows a stacked co-addition of all 17 deep integration cluster fields discussed in Section 3.3. The weight function used in the stack is the expected y_0 based on the measured $T_{\rm e}$ in the cluster. The cluster maps are all centred on $\Delta\alpha = 0, \Delta\delta = 0$ so the imaged SZ effects should all be centred at the same point. The image grey scaling is from -2 mJy to 2 mJy, and contours are plotted at $\{-1.0, -0.5\}$ mJy (dotted) and $\{0.5, 1.0, 1.5\}$ mJy (dashed). The statistical noise in this map is $1\sigma = 0.2$ mJy at the centre of the field, and the map has been apodized using the summed hit map. The box at upper right contains an artificial point source with peak brightness equal to that of the SZ effect in this map (1.83 mJy) as a reference for the emission at the centre of the co-addition, which in comparison is quite extended.

deviation of the per cent change for the set). A decrease in $\theta_{\rm c}$ by the same factor – that is, increasing the 'peakiness' of the clusters by a considerable amount – leads to a change in the average y_0 of 2 ± 4 per cent. Alternatively, the fit amplitudes are a stronger function of β: increasing β by a factor of 2 leads to a 25 ± 7 per cent decrease in the measured ΔI_0. Clearly, a moderate misestimation of the model can have an appreciable affect on the y_0 measurements discussed here.

An issue related to the cluster flux distribution model is that of cooling flows: such clusters have more peaked centres than their approximately isothermal counterparts. In the set of clusters shown in Fig. 6, Abell 1689, Abell 2390 and RXJ $1347-1145$ are classed as clusters having cooling cores. Although at least 2 of these 3 clusters exhibit SCUBA–determined y_0 significantly higher than that measured at the decrement, this is not statistically different than for the non-cooling flow clusters. More data would be required to reliably differentiate between these cluster types.

Interestingly, Fig. 5 suggests that the centres of our cluster sample, on average, emit a factor of 2 more flux at $850\ \mu$m than the SZ models used here can account for. This flux may in fact be the signature of excess emission from cooling flow core clusters in the total cluster sample of 17 fields, or a more generic failure of the isothermal β model. Equally, it could be the signature of dim point sources in these clusters. It is not possible to differentiate between these options with the data at hand.

Finally, two components of the analysis pipeline could have a systematic effect on the final amplitudes, the first of these being calibration. We have used the SCUBA calibration observations determined between 2 and 5 times nightly at the JCMT to calibrate the observations presented here. Although it is difficult to model how the calibrations could be systematically incorrect by an appreciable factor, there is certainly an approximately 10 per cent variation in the calibration runs taken over a single night. For deep cluster fields, this effect should average out; however, for shallow fields this may not be true. Fortunately, the 8 deep fields discussed in this section should not suffer from systematic calibration problems. A second component of the analysis pipeline which may systematically affect the measured y_0 is the correction for the $450\ \mu$m atmosphere subtraction. Although the size of the correction is typically less than 10 per cent, it may help artificially increase the measured y_0 if the correction algorithm is erroneous. We have attempted to be completely consistent with the $450\ \mu$m correction, but as it is itself based on the SZ effect model, the correction does increase the systematic uncertainty of the measurement.

As a final comparison, we can consider the amplitudes determined by Zemcov et al. (2003) for Cl $0016+16$ and MS $1054-03$.

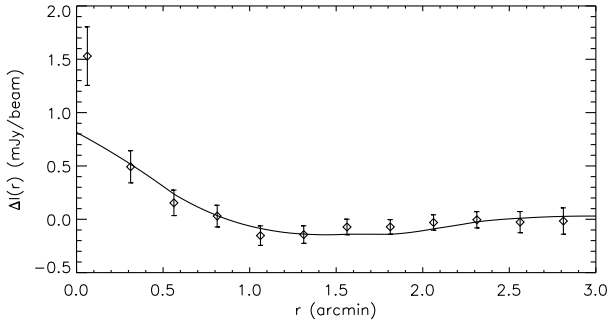

Figure 5. Radial averages of the model and data coadded maps for the 17 deep integration time cluster fields. The diamond points show the averages of the stacked data map (shown in Figure 4) in annular bins with width 15 arcsec (a SCUBA beam). The error bars are similarly determined from the stacked variance map. The model, shown as a solid line, is determined by creating a simulated 'map' for each cluster, sampling it according to the telescope's recorded pointing, and running the resulting time series through the data analysis pipeline to create maps which reflect the spatial filtering of SCUBA's chopping pattern and the pipeline itself. These individual model maps are then stacked using the same noise weights as are applied to the data map stack, and the resulting map is averaged in annuli. To apply the proper normalization, the model averages are fit to the data averages before plotting. This figure shows that the model and data agree quite well, except in the central bin, where the measured flux exceeds the model expectation by a factor of ~ 2.

In that work, the measured y_0 from the SCUBA data alone were $(2.2 \pm 0.7) \times 10^{-4}$ and $(2.0 \pm 1.0) \times 10^{-4}$, respectively. Although these values are different than those listed in Table 3, the disparity is not statistically significant.

4.2 Point sources

As part of this survey of archival SCUBA data, we have presented a list of point source candidates found in our maps. Broadly, these fall into three categories: bright central sources associated with AGN activity in the cluster's central galaxy; lensed sources in moderate and high redshift clusters; and star forming sources in the clusters themselves. Sources belonging to the first category are generally very easy to identify, as they correspond to well known galaxies at other wavelengths (e.g. Hydra A). The second category have typically already been well studied, as in Abell 2218 (Kneib et al. 2004b) and MS $0451-0305$ (Borys et al. 2004), and correspond to sources around $z \simeq 2$–3 (Smail et al. 1997, Chapman et al. 2002). Such lensed sources are common in rich cluster fields; most clusters with long integration times exhibit this type of source.

Low signal-to-noise sources in a population with steep source counts tend to appear somewhat brighter than they actually are. One can attempt to correct for this by performing a flux de-boosting procedure (e.g. Coppin et al. 2005). We have not done this for our source list, since the procedure would be complicated for such an inhomogeneous data-set, and would also depend on modeling the lensing effects. It is therefore important to appreciate that the fluxes given in Table 5 will generally be biased high, this being particularly true for the low significance sources.

4.3 Future experiments

It is problematic for this type of measurement that, for a given cluster, background source lensing and the amplitude of the SZ effect are highly correlated. In other words, a massive cluster with a large SZ effect is also a strong lensing cluster. This underscores the need for experiments with high spatial resolution and multi-wavelength coverage, particularly at sub-mm wavelengths. Although the peak of the SZ effect and that of maximum lensing have different spatial shapes, an instrument like SCUBA – with its single SZ effect observation frequency and relatively poor spatial resolution – will have trouble disentangling the effects in clusters where the SZ shape is broad.

Nevertheless, the measurements presented here are instructive. They show that it is possible to provide useful constraints on the SZ increment using mm/sub-mm array receivers and highlight the most likely sources of systematic error in any sub-mm SZ effect experiment: chopping effects (necessitated by the strongly varying atmosphere in the sub-mm regime) and the contamination of point sources, particularly lensed ones, which are thought to be correlated with the existence of a strong SZ cluster. We have shown that one must to try to remove the effects of bright point source contamination in these type of measurements, and that when chopped data are used one must be careful to compensate for the effects of chopping as much as possible in order not to remove a significant part of the signal.

In the future, the combination of SZ data at a range of wavelengths (from 10s of GHz to 400 GHz or higher), together with X-ray, lensing and other optical studies, should allow for constraints to be placed on the kinetic SZ effect. This effect will yield the radial velocity of the cluster which, in principle, will constrain large scale flows in the Universe. Multi-wavelength SZ data will also be useful for studies of cluster astrophysics, from temperature and mass determinations to sub–structure within the cluster gas itself.

The next generation camera for the JCMT, SCUBA-2 (Holland et al. 2003, Holland et al. 2006) will alleviate many of the problems with SZ effect increment measurements highlighted by this work. SCUBA-2 will bring CCD-style imaging to sub-mm astronomy; sampling at 200 Hz, it will allow imaging of the sky much faster than atmospheric variation ($\simeq 1$ Hz). The large array coupled with rapid scanning and map-making techniques should allow for a robust estimate of modes on scales many times larger than SCUBA-1 has permitted. Since typical increment amplitudes for rich clusters correspond to ~ 1 mJy per $850\,\mu$m JCMT beam with a spatial shape spread over tens of beams, high signal-to-noise ratio SZ measurements of targeted clusters should be possible. Weaker statistical measurements of less massive clusters may also be possible in 'blank sky' surveys. Despite the improvements in mapping structure over many arc minutes, SCUBA-2's resolution will be the same as SCUBA's, and hence lensed sub-mm sources will still be an issue. However, with SCUBA-2's much higher sensitivity, their identification and removal should be simpler. And obviously the availability of deep data at other wavelengths will be crucial for extracting lensed sources. Candidate lensed sources in cluster fields can be followed up with pointed observations with much higher resolution using existing interferometers, and eventually the full power of ALMA. When point source free high frequency SCUBA-2 data are combined with those from the next generation of dedicated SZ effect experiments very powerful constraints on the full SZ effect spectrum in hundreds of clusters should become commonplace.

ACKNOWLEDGMENTS

Many thanks to the anonymous MNRAS referee whose insightful comments helped substantially improve this paper. Also, we are

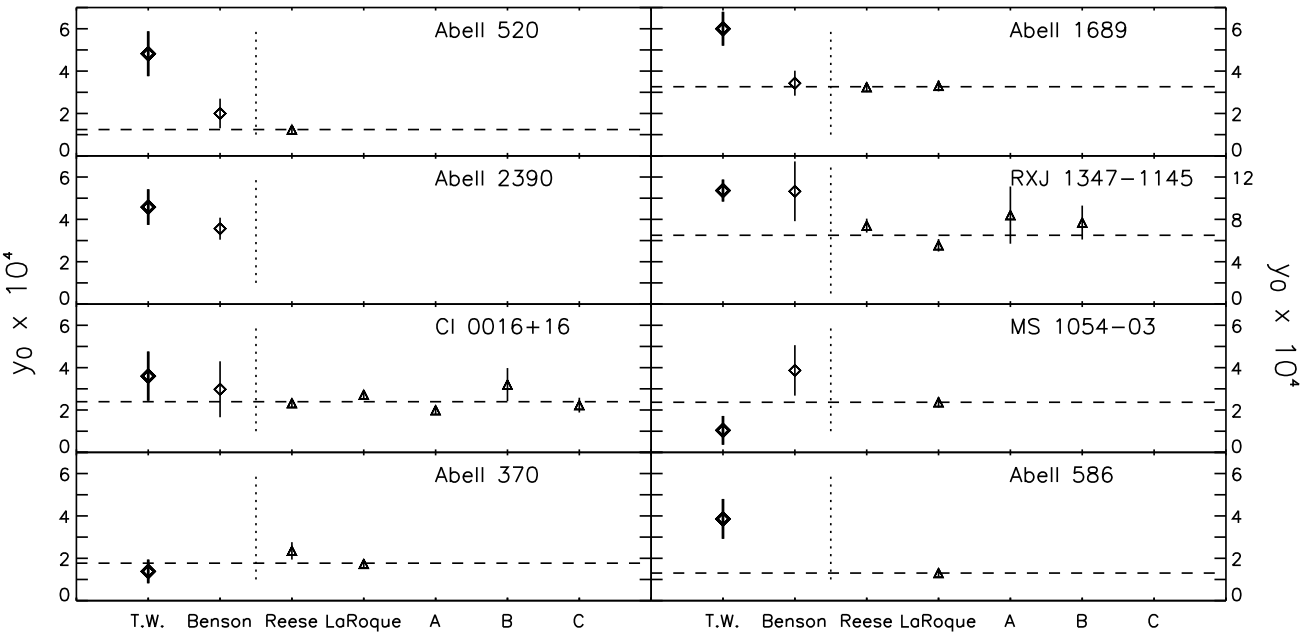

Figure 6. Comparison of the measurements in this work with those available in the literature. Each panel shows the results for one cluster; the y axis gives the measured y_0 and its associated 68 per cent confidence interval as quoted in the references as labeled on the x axis. These references are as follows: 'T. W.' is this work (shown as heavy points), 'Benson' is Benson et al. (2004), 'Reese' is Reese et al. (2002), and 'LaRoque' is LaRoque et al. (2006). For Cl $0016+16$ reference 'A' is Grainge et al. (2002), 'B' is Desert et al. (1998) and 'C' is Hughes & Birkinshaw (1998), while for RXJ $1347-1145$ reference 'A' is Pointecouteau et al. (2001) and 'B' is Komatsu et al. (2001). In these plots, measurements using the SZ increment are plotted as diamonds and measurements in the decrement are plotted as triangles; the types of measurement are separated by the vertical dotted line in each panel. The horizontal dashed line shows the weighted mean of the decrement measurements (i.e. triangles) only. Interestingly, the points measured using the SZ increment tend to lie at larger y_0 than their decrement counterparts; this may be indicative of point source contamination.

extremely grateful to S. Church for her repeated and kind hosting and loan of computers during the course of this work.

This work was funded by the Natural Sciences and Engineering Research Council of Canada. The James Clerk Maxwell Telescope is operated by the Joint Astronomy Centre on behalf of the Particle Physics and Astronomy Research Council of the United Kingdom, the Netherlands Organization for Scientific Research, and the National Research Council of Canada. This work made use of the Canadian Astronomy Data Centre, which is operated by the Herzberg Institute of Astrophysics, National Research Council of Canada. This research has made use of data obtained from the High Energy Astrophysics Science Archive Research Center (HEASARC), provided by NASA's Goddard Space Flight Center.

REFERENCES

Allen S. W., Fabian A. C., 1998, MNRAS, 297, L57
Allen S. W., 2000, MNRAS, 315, 269
Allen S. W., Schmidt R. W., Fabian A. C., 2002, MNRAS, 335, 256
Archibald E. N. et al., MNRAS, 336, 1
Baker J. E., Myers S. T., Readhead A. C. S., Herbig T., 1994, Bulletin of the American Astronomical Society, 26, 1410
Barger A. J., Cowie L. L., Smail I., Ivison R. J., Blain A. W., Kneib J.-P., 1999, AJ, 117, 2656
Bennett C. L. et al., 2003, ApJS, 148, 97
Benson B. A., Church S. E., Ade P. A. R., Bock J. J., Ganga K. M., Henson C. N., Thompson K. L., 2004, ApJ, 617, 829
Benson B. A. et al., 2003, ApJ, 592, 674
Best P. N., 2002, MNRAS, 336, 1293
Best P. N., van Dokkum P. G., Franx M., Röttgering H. J. A., 2002, MNRAS, 330, 17
Birkinshaw M., Gull S. F., Moffet A. T., 1981, ApJL, 251, L69
Birkinshaw M., Gull S. F., Hardebeck H., 1984, Nature, 309, 34
Birkinshaw M., 1999, Phys. Reports, 310, 97
Biviano A., et al., 2004, A & A, 425, 33
Böhringer H., et al., 2000, ApJS, 129, 435
Borys C., Chapman S. C., Scott D., 1999, MNRAS, 308, 527
Borys C., et al., 2004, MNRAS, 352, 759
Carlstrom J. E., Joy M., Grego L., 1996, ApJL, 456, L75
Carlstrom J. E., Holder G. P., Reese E. D., 2002, Annual Rev. Astron. & Astrophys., 40, 643
Chapman S. C., Scott D., Borys C., Fahlman G. G., 2002, MNRAS, 330, 92
Chase S. T., Joseph R. D., Robertson N. A., Ade P. A. R., 1987, MNRAS, 225, 171
Cooray A. R., Grego L., Holzapfel W. L., Joy M., Carlstrom J. E., 1998, AJ, 115, 1388
Coppin K., Halpern M., Scott D., Borys C., Chapman S., 2005, MNRAS, 357, 1022
Cowie L. L., Barger A. J., Kneib J.-P., 2002, ApJ, 123, 2197
Cox C. V., Bregman J. N., Schombert J. M., 1995, ApJS, 99, 405
Crawford C. S., Allen S. W., Ebeling H., Edge A. C., Fabian A. C., 1999, MNRAS, 306, 857
Cruddace R., et al., 2002, ApJS, 140, 239
David L. P., Forman W., Jones C., 1999, ApJ, 519, 533
De Filippis E., Schindler S., Castillo-Morales A., 2003, A & A,

404, 63
de Plaa J., Kaastra J. S., Tamura T., Pointecouteau E., Mendez M., Peterson J. R., 2004, A & A, 423, 49
Desert F.-X., et al., 1998, New Astronomy, 3, 655
Donahue M., Gaskin J. A., Patel S. K., Joy M., Clowe D., Hughes J. P., 2003, ApJ, 598, 190
Duc P.-A., et al., 2002, A & A, 382, 60
Durret F., Adami C., Gerbal D., Pislar V., 2000, A & A, 356, 815
Ebeling H., Edge A. C., Bohringer H., Allen S. W., Crawford C. S., Fabian A. C., Voges W., Huchra J. P., 1998, MNRAS, 301, 881
Edge A. C., Ivison R. J., Smail I., Blain A. W., Kneib J.-P., 1999, MNRAS, 306, 599
Edge A. C., 2001, MNRAS, 328, 762
Egami E., et al., 2005, ApJL, 618, L5
Ettori S., Fabian, A. C., 1999, MNRAS, 305, 834
Ettori S., Tozzi P., Borgani S., Rosati P., 2004, A & A, 417, 13
Frayer D. T., Smail I., Ivison R. J., Scoville N. Z., 2000, ApJ, 120, 1668
Gioia I. M., Luppino G. A., 1994, ApJS, 94, 583
Gioia I. M., Shaya E. J., Le Fevre O., Falco E. E., Luppino G. A., Hammer F., 1998, ApJ, 497, 573
Gioia I. M., Braito V., Branchesi M., Della Ceca R., Maccacaro T., Tran K.-V., 2004, A & A, 419, 517
Gladders M. D., Yee H. K. C., 2005, ApJS, 157, 1
Govoni F., Markevitch M., Vikhlinin A., VanSpeybroeck L., Feretti L., Giovannini G., 2004, ApJ, 605, 69
Grainge K., Jones M., Pooley G., Saunders R., Edge A., 1993, MNRAS, 265, L57
Grainge K., Grainger W. F., Jones M. E., Kneissl R., Pooley G. G., Saunders R., 2002, MNRAS, 329, 890
Grego L., Carlstrom J. E., Joy M. K., Reese E. D., Holder G. P., Patel S., Cooray A. R., Holzapfel W. L., 2000, ApJ, 539, 39
Grego L., Carlstrom J. E., Reese E. D., Holder G. P., Holzapfel W. L., Joy M. K., Mohr J. J., Patel S., 2001, ApJ, 552, 2
Griffith M. R., Wright A. E., Burke B. F., Ekers R. D., 1994, ApJS, 90, 179
Gunn J. E., Hoessel J. G., Oke J. B., 1986, ApJ, 306, 30
Hicks A. K., Wise M. W., Houck J. C., Canizares C. R., 2002, ApJ, 580, 763
Holland W. S. et al., 1999, MNRAS, 303, 659
Holland W. S., Duncan W., Kelly B. D., Irwin K. D., Walton A. J., Ade P. A. R., Robson E. I., 2003, Proceedings of the SPIE, 4855, 1
Holland W. S. et al., 2006, Proceedings of the SPIE, 6275, 45
Holzapfel W. L., 1996, PhD Thesis, Univ. California
Holzapfel W. L., Ade P. A. R., Church S. E., Mauskopf P. D., Rephaeli Y., Wilbanks T. M., Lange A. E., 1997, ApJ, 481, 35
Hughes J. P., Birkinshaw M., 1998, ApJ, 501, 1
Itoh N., Kohyama Y., Nozawa S., 1998, ApJ, 501, 7
Ivison R. J., Smail I., Le Borgne J.-F., Blain A. W., Kneib J.-P., Bezecourt J., Kerr T. H., Davies J. K., 1998, MNRAS, 298, 583
Ivison R. J., Smail I., Barger A. J., Kneib J.-P., Blain A. W., Owen F. N., Kerr T. H., Cowie L. L., 2000, MNRAS, 315, 209
Jeltema T. E., Canizares C. R., Bautz M. W., Malm M. R., Donahue M., Garmire G. P., 2001, ApJ, 562, 124
Jenness T., Stevens J. A., Archibald E. N., Economou F., Jessop N. E., Robson E. I., 2002, MNRAS, 336, 14
Jones M., et al., 1993, Nature, 365, 320
Jones M. E., et al., 2005, MNRAS, 357, 518
Joy M. et al., 2001, ApJL, 551, L1
Kneib J.-P., Ellis R. S., Santos M. R., Richard J., 2004, ApJ, 607, 697
Kneib J.-P., van der Werf P. P., Kraiberg Knudsen K., Smail I., Blain A., Frayer D., Barnard V., Ivison R., 2004, MNRAS, 349, 1211
Knudsen K. K., van der Werf P. P., Jaffe W., 2003, A & A, 411, 343
Knudsen K. K. et al., 2005, ApJL, 632, L9
Komatsu E., Kitayama T., Suto Y., Hattori M., Kawabe R., Matsuo H., Schindler S., Yoshikawa K., 1999, ApJL, 516, L1
Komatsu E., et al., 2001, PASJ, 53, 57
Lamarre J. M., et al., 1998, ApJL, 507, L5
Lancaster K., et al., 2005, MNRAS, 359, 16
LaRoque S. J., et al., 2003, ApJ, 583, 559
LaRoque S. J., Bomamente J., Carlstrom J., Joy M., Nagai D., Reese E., Dawson K., 2006, ApJ, 652, 917
Lubin L. M., Brunner R., Metzger M. R., Postman M., Oke J. B., 2000, ApJL, 531, L5
Machacek M. E., Bautz M. W., Canizares C., Garmire G. P., 2002, ApJ, 567, 188
Majerowicz S., Neumann D. M., Reiprich T. H., 2002, A & A, 394, 77
Mason B. S., Myers, S. T., 2000, ApJ, 540, 614
Mason B. S., Myers S. T., Readhead A. C. S., 2001, ApJL, 555, L11
Maughan B. J., Jones L. R., Ebeling H., Perlman E., Rosati P., Frye C., Mullis C. R., 2003, ApJ, 587, 589
Mauskopf P. D., et al., 2000, ApJ, 538, 505
Metcalfe L., et al., 2003, A & A, 407, 791
Mohr J. J., Reese E. D., Ellingson E., Lewis A. D., Evrard A. E., 2000, ApJ, 544, 109
Myers S. T., Baker J. E., Readhead A. C. S., Leitch E. M., Herbig T., 1997, ApJ, 485, 1
Ota N., Mitsuda K., Fukazawa Y., 1998, ApJ, 495, 170
Ota N., Mitsuda K., 2004, A & A, 428, 757
Ota N., Pointecouteau E., Hattori M., Mitsuda K., 2004, ApJ, 601, 120
Pointecouteau E., Giard M., Benoit A., Désert F. X., Aghanim N., Coron N., Lamarre J. M., Delabrouille J., 1999, ApJL, 519, L115
Pointecouteau E., Giard M., Benoit A., Désert F. X., Bernard J. P., Coron N., Lamarre J. M., 2001, ApJ, 552, 42
Pointecouteau E., Arnaud M., Kaastra J., de Plaa J., 2004, A & A, 423, 33
Postman M., Lubin L. M., Oke J. B., 2001, AJ, 122, 1125
Pratt G. W., Böhringer H., Finoguenov A., 2005, A & A, 433, 777
Privett G., Jenness T., Matthews H. E., 1998, Fluxes - JCMT position and flux density calibration. Starlink User Note 213, Starlink Project, CLRC
Radford S. J. E., Boynton P. E., Ulich B. L., Partridge R. B., Schommer R. A., Stark A. A., Wilson R. W., Murray S. S., 1986, ApJ, 300, 159
Reese E. D., Carlstrom J. E., Joy M., Mohr J. J., Grego L., Holzapfel W. L., 2002, ApJ, 581, 53
Reese E. D., et al., 2000, ApJ, 533, 38
Reiprich T. H., Böhringer H., 2002, ApJ, 567, 716
Rizza E., Burns J. O., Ledlow M. J., Owen F. N., Voges W., Bliton M., 1998, MNRAS, 301, 328
Romer A. K. et al., 2000, ApJS, 126, 209
Rosati P., Della Ceca R., Norman C., Giaconni R., 1998, ApJ, 492, L21
Rosati P., Stanford S. A., Eisenhardt P. R., Elston R., Spinrad H., Stern D., Dey A., 1999, AJ, 118, 76

Sanders J. S., Fabian A. C., Allen S. W., 2000, MNRAS, 318, 733
Saunders R., et al., 2003, MNRAS, 341, 937
Sarazin C. L., 1988, X-ray emissions from clusters of galaxies. Cambridge Univ. Press, Cambridge
Scharf C., Jones L. R., Ebeling H., Perlman E., Malkan M., Wenger G., 1997, ApJ, 477, 79
Schmidt R. W., Allen S. W., Fabian A. C., 2001, MNRAS, 327, 1057
Sheth K., Blain A. W., Kneib J.-P., Frayer D. T., van der Werf P. P., Knudsen K. K., 2004, ApJL, 614, L5
Smail I., Ivison R. J., Blain A. W., 1997, ApJL, 490, L5
Smail I., Ivison R. J., Blain A. W., Kneib J.-P., 2002, MNRAS, 331, 495
Smail I., Smith G. P., Ivison R. J., 2005, ApJ, 631, 121
Soucail G., Ota N., Böhringer H., Czoske O., Hattori M., Mellier Y., 2000, A & A, 355, 433
Spergel D. N., et al., 2006, ApJ, Submitted (astro-ph/0603449)
Stickel M., Klaas U., Lemke D., Mattila K., 2002, A & A, 383, 367
Sun M., Jones C., Murray S. S., Allen S. W., Fabian A. C., Edge A. C., 2003, ApJ, 587, 619
Sunyaev R., Zel'dovich Y., 1972, Comments Astrophys. Space Phys., 4, 173
Tsuboi M., Miyazaki A., Kasuga T., Matsuo H., Kuno N., 1998, PASJ, 50, 169
Udomprasert P. S., Mason B. S., Readhead A. C. S., Pearson T. J., 2004, ApJ, 615, 63
Ueda Y., Ishisaki Y., Takahashi T., Makishima K., Ohashi T., 2001, ApJS, 133, 1
Uyaniker B., Reich W., Schlickeiser R., Wielebinski R., 1997, A & A, 325, 516
Véron-Cetty, M.-P., & Véron, P. 2001, A & A, 374, 92
Vikhlinin A., VanSpeybroeck L., Markevitch M., Forman W. R., Grego L., 2002, ApJL, 578, L107
Vlahakis C., Dunne L., Eales S., 2005, MNRAS, 364, 1253
Webb T. M. A., Yee H. K. C., Ivison R. J., Hoekstra H., Gladders M. D., Barrientos L. F., Hsieh B. C., 2005, ApJ, 631, 187
Wiedner M. C., Hills R. E., Carlstrom J. E., Lay O. P., 2001, ApJ, 553, 1036
Wilbanks T. M., Ade P. A. R., Fischer M. L., Holzapfel W. L., Lange A. E., 1994, ApJL, 427, L75
Worrall D. M., Birkinshaw M., 2003, MNRAS, 340, 1261
Xue S., Wu X., 2002, ApJ, 576, 152
Zemcov M., Halpern M., Borys C., Chapman S., Holland W., Pierpaoli E., Scott D., 2003, MNRAS, 346, 1179
Zemcov M., Halpern M., Pierpaoli E., 2005, MNRAS, 359, 447

APPENDIX A

Table 4: Archival cluster data sets. Listed are the clusters, JCMT project IDs, dates and integration times. We also give the mean and scatter of the optical depth for the uncorrupted parts of the data sets. For sets with insufficient τ_{850} measurements to measure the scatter, the $\sigma(\tau_{850})$ column is left blank.

Cluster	Project IDs	Observation dates	Integration time (ks)	$\langle\tau_{850}\rangle$	$\sigma(\tau_{850})$
Abell 68	M01AU01	Feb. 22, 2001 and Jan. 4 & 10, 2002	12.2	0.40	0.04
Abell 85	M98AU60	Apr. 19, Jun. 07, 1998	9.7	0.46	0.08
	M98SU60	Jun. 16, 1998	1.0	0.29	
	Combined		10.7	0.44	0.09
Abell 209	M01AU01	Aug. 22, 23 & Nov. 23, 2001	24.3	0.43	0.05
Abell 222	M98AU17	Jul. 02 & Nov. 29, 1998	9.6	0.20	0.12
Abell 370	U45	Jul. 02, 03, 04 & 05, 1997	25.7	0.26	0.06
	M97BH13	Oct. 30, 1997	6.3	0.27	0.08
	M97BU33	Aug. 09, 1997	7.7	0.27	0.02
	M99BH02	Aug. 24, 25, 26 & 27, 1999 and Nov. 12 & 13, 1999	69.2	0.22	0.12
	M00BH04	Nov. 27 & 29, 2000	5.1	0.36	0.06
	M00BUHFLEX	Dec. 08 & 09, 2000 and Jan. 07 & 09, 2001	21.8	0.37	0.11
	Combined		135.8	0.26	0.12
Abell 383	M00BU18	Feb. 28, 2001	3.8	0.26	0.02
	M01AU01	Feb. 22, Mar. 02 and Jul. 26, 2001	7.0	0.40	0.01
	M02BH46A	Jan. 06, 2003	5.1	0.112	0.01
	M03AH15A	Feb. 18 & 20, May 19 and Jun. 03, 2003	18.0	0.17	0.05
	M03BH25A	Aug. 19, 2003	2.6	0.30	0.01
	Combined		36.6	0.20	0.09
Abell 478	M97AN15	Sept. 07 and Dec. 06, 1997	9.0	0.71	0.39
	M98BU67	Mar. 10 & 11, 1998	12.8	0.22	0.03
	M99BN13	Dec.06, 1999	2.6	0.27	0.01
	Combined		24.4	0.49	0.37
Abell 496	M98BN02	Nov. 14, 24, & 25, 1998	20.1	0.22	0.07
	M99BN13	Aug. 07 & 08, 1999	15.4	0.28	0.03
	Combined		35.5	0.25	0.06
Abell 520	M98AU17	Jul. 24, 25, 31 & Nov. 29, 1998	30.6	0.27	0.07
	M98BN02	Jan. 30, 1999	11.5	0.26	0.03
	M00BN12	Dec. 19, 20 & 21, 2000	19.2	0.31	0.04
	Combined		61.3	0.29	0.06
Abell 586	M98AU17	Apr. 21, Sept. 12, Oct. 31, & Nov. 01, 1998	21.1	0.19	0.08
Abell 665	M00AU09	Nov. 17, 2000	1.3	0.31	
	M00BU18	Nov. 17, 2000	6.4	0.32	0.01
	Combined		7.7	0.32	0.01
Abell 773	M01AU01	Feb. 22 and Mar. 03, 2001	23.3	0.39	0.03
Abell 780	M98BN02	Sept. 20, 1998	2.6	0.31	
Abell 851	M98AU39	Mar. 12 & 13, 1998	30.1	0.23	0.15
	M00BH05	Dec. 27, 28, 29, 30 & 31, 2000 and Jan. 01 & 09, 2001	39.7	0.25	0.05
	M01AUHFLEX	Mar. 30 & 31, 2001	10.3	0.25	0.05
	Combined		80.1	0.25	0.08
Abell 963	M00AU09	Feb. 28 and Mar. 1 & 2, 2001	9.6	0.33	0.03

Continued on next page

Table 4 – continues from previous page

Cluster	Project IDs	Observation dates	Integration time (ks)	$\langle\tau_{850}\rangle$	$\sigma(\tau_{850})$
	M00BU18	Nov. 17, 2000	5.1	0.31	
	M01AU01	May 7, 2001	5.1	0.48	0.07
	M02BH46A	Dec. 6, 22, 28, 29 & 30, 2002 and Jan. 06, 2003	57.3	0.19	0.06
	M03BH25A	Oct. 03, 2003	2.6	0.30	
	M04AH19A	Mar. 9, 2004	3.1	0.33	0.01
	Combined		82.8	0.24	0.10
Abell 1689	M98AU17	Apr. 21, 1998	8.2	0.18	0.02
	M98AU27	Feb. 26, 27 & Nov. 25, 1998	23.0	0.14	0.04
	M99AU46	Dec. 27, 1999	7.7	0.27	0.06
	M99BN13	Dec. 06, 07, 08 & 14, 1999	35.2	0.37	0.15
	SCUBA	Jun. 30, 1999	6.4	0.22	0.06
	Combined		80.5	0.26	0.14
Abell 1763	M01AU01	May 15 & 16, 2001	14.8	0.45	0.06
Abell 1835	M97BI16	Jan. 31 & Feb. 01, 1998	13.4	0.17	0.04
	M98AU39	Apr. 03, 1998	9.6	0.20	0.02
	Combined		23.0	0.18	0.04
Abell 1914	M98AU27	Feb. 26, 1998	3.8	0.12	0.01
Abell 2163	M98AC31	Jun. 28, 29 & 30, 1998	7.2	0.17	0.03
	M98AU27	Feb. 26 & 27, 1998	3.8	0.12	0.03
	Combined		11.0	0.15	0.04
Abell 2204	M98AU60	Feb. 10, 1998	5.2	0.38	0.01
Abell 2218	M98AN14	Mar. 20 & 22, 1998	19.8	0.39	0.03
	M00BN11	Jan. 27 & 29, 2001	19.2	0.20	0.02
	M00BU38	Aug. 09, 11, 12 & 13, 2000	55.9	0.23	0.10
	M01BN21	Jan. 05, 06 & 07, 2002	28.8	0.34	0.09
	Combined		123.7	0.27	0.10
Abell 2219	M98AC41	Apr. 05, 1998	16.1	0.17	0.02
	M00BN12	Jan. 26, 2001	14.7	0.16	0.04
	Combined		30.8	0.17	0.04
Abell 2261	M98BC32	Jan. 30 & Feb. 26, 1999	4.9	0.14	
Abell 2390	M97BU33	Aug. 10, 11, 12, 14, 21, & 22, and Dec.19, 1997	27.6	0.28	0.07
	M98AU39	Apr. 03, 1998	6.6	0.15	0.01
	M99BH04	Sept. 02, 03, 04, 08 and Nov. 12 & 13, 1999	37.6	0.28	0.14
	M00BUHFLEX	Dec. 08, 2000	2.6	0.44	0.03
	M01AUHFLEX	Jun. 17, 18, 19, 2001	24.2	0.44	0.08
	Combined		98.7	0.33	0.13
Abell 2597	M98BN02	Nov. 14, 15, 24, & 25, 1998	23.0	0.23	0.09
Cl 0016+16	M98AC41	Apr. 05, Sept. 02, 1998	13.0	0.24	0.01
	M98BC32	Sept. 03,1998	5.8	0.42	0.01
	M99BC41	Nov. 11, 1999	7.2	0.31	0.03
	M00BU18	Oct. 13, 2000	2.6	0.37	
	M02BC37	Oct. 03, 2002	2.1	0.29	0.01
	Combined		30.6	0.31	0.10
Cl 0023+0423	M00BN17	Oct. 25, 2000	16.6	0.33	0.04
	M01BU01	Sept. 26, 30 & Nov. 15, 2001	20.1	0.28	0.07
	N01BU01	Dec. 08, 2001	11.5	0.24	0.05
	Combined		48.3	0.29	0.07
Cl 0024+1652	M97BU33	Aug. 14 & Dec. 19, 1997 and Jan. 26, 1998	14.3	0.20	0.06

Continued on next page

Table 4 – continues from previous page

Cluster	Project IDs	Observation dates	Integration time (ks)	$\langle\tau_{850}\rangle$	$\sigma(\tau_{850})$
	M02BH46A	Aug. 08, 2002	0.4	0.82	
	M03AH15A	Jun. 03, 2003	2.6	0.24	0.02
	Combined		17.3	0.26	0.18
Cl 0055−2754	M01AU01	Jan. 10, 2002	2.6	0.33	
Cl 0152−1357	M03BC31	Sept. 28, 29 & Oct. 17, 2003	13.4	0.23	0.03
Cl 0303+1706	M01AU01	Aug. 11, 12 & Nov. 23, 2001	13.2	0.49	0.07
Cl 0848+4453	M00AN22	Feb. 26, 27 & 28, 2000	29.2	0.27	0.03
Cl 1455+2232	M97BC45	Jan. 04, 1998	15.3	0.15	0.02
Cl 1604+4304	M00AN22	Mar. 03, 04, 21 & 22, 2000	41.6	0.17	0.07
Cl 1604+4321	M00BN17	Oct. 25, 2000 & Jan. 28, 2001	14.1	0.19	0.07
Cl 2129+0005	M98AU27	Feb. 27, 1998	2.6	0.11	0.06
Cl 2244−0221	U45	Jul. 02, 03, 04 & 05, 1997	23.0	0.25	0.06
	M98AU39	Apr. 03, 1998	2.6	0.12	0.00
	Combined		25.6	0.24	0.07
MS 0440+0204	M97BU33	Aug. 09, 10, 12, 13 and Sept. 22 & Dec. 19, 1997	31.4	0.35	0.13
	M98AU39	Mar. 12 & 13, 1998	7.0	0.27	0.03
	Combined		38.4	0.32	0.13
MS 0451−0305	M98AC41	Sept. 02, 1998	1.5	0.43	
	M98BC32	Sept. 03, 1998	14.1	0.41	0.01
	M99BC41	Nov. 10 & 11, 1999	14.7	0.31	0.03
	M00BU18	Nov. 19, 2001	5.1	0.37	0.01
	Combined		35.5	0.36	0.06
MS 1054−0321	M98AC31	Jun. 28, 1998	2.6	0.22	
	M98AC37	May 14, 1998	5.1	0.33	
	M98BN02	Nov. 14, 29 & 30, 1998	23.0	0.24	0.12
	M99BC41	Nov. 10 & 11, 1999	14.7	0.31	0.03
	M99BN13	Dec. 06, 07, 08, and 14, 1999	17.9	0.35	0.11
	M02AN12	Apr. 10, 14, 15, and 16, 2002	46.7	0.32	0.07
	M03AN18	Dec. 23, 24, 26, 27, 2002 and Jan. 28, Apr. 23, 24, 25, 26, 27, & May 19, 2003	75.6	0.27	0.11
	Combined		167.7	0.29	0.10
PKS 0745−19	M97AN15	Sept. 12, 1997	6.4	0.36	0.04
	M00BU18	Sept. 20, 2000	2.6	0.13	
	Combined		9.0	0.32	0.10
RXJ 1347−1145	M98AI18	May 31 & Jun. 01, 1998	17.0	0.56	0.07
	M99AU77	Jul. 03 & 04, 1999	6.1	0.42	0.24
	M00BN12	Dec. 19,20,21, 2000 and Jan. 25, 2001	17.9	0.31	0.05
	SCUBA	Dec. 21, 2000	0.4	0.33	0.04
	Combined		53.0	0.35	0.16
Zwicky 3146	m98ac41	Apr. 08 & 09, 1998	7.2	0.16	0.04
	m98bc32	Jan. 28, 1999	5.1	0.18	0.04
	Combined		12.3	0.16	0.03

APPENDIX B

Table 5: Positions, fluxes at $850\,\mu$m and $450\,\mu$m, errors and χ^2 statistics for the candidate sources. The χ^2 values are determined by subtracting the fiducial JCMT PSF from the map centred on the nominal point source's position and then summing the squared residuals for the entire image. Sources which may be images of the SZ effect are marked; these are *not* subtracted before the SZ effect fit discussed in Section 3. Because the $450\,\mu$m SCUBA array is smaller than the $850\,\mu$m array, some sources at the edge of the $850\,\mu$m map do not appear in the $450\,\mu$m map; these are donoted with the label 'Off Edge' in the $450\,\mu$m flux column.

Cluster Source	α_{2000} (hh:mm:ss)	δ_{2000} (+dd:mm:ss)	$850\,\mu$m Flux (mJy)	$850\,\mu$m S/N	χ^2 / Degrees of Freedom	$450\,\mu$m Flux (mJy)
Abell 209-1	1:31:51.3	−13:37:45	10.7	3.4	171 / 177	65±273
Abell 370-1	2:39:51.9	−01:35:55	20.5	19.9	403 / 177	−2±19
Abell 370-2	2:39:57.6	−01:34:50	6.8	7.8	186 / 177	1±12
Abell 370-3	2:39:56.3	−01:34:25	6.2	6.5	230 / 177	6±6
Abell 370-4	2:39:54.0	−01:33:34	4.0	4.1	176 / 177	1±3
Abell 370-5[a]	2:39:52.9	−01:35:04	3.0	4.1	142 / 177	1±5
Abell 383-1[a]	2:48:02.9	−03:31:47	5.5	4.2	156 / 177	−23±22
Abell 478-1	4:13:26.9	+10:27:41	30.0	16.2	283 / 177	11±33
Abell 478-2	4:13:28.2	+10:28:03	10.8	4.2	302 / 177	0±20
Abell 478-3	4:13:23.4	+10:26:54	7.4	3.5	151 / 177	3±24
Abell 496-1	4:33:37.6	−13:15:45	8.9	7.8	179 / 177	3±12
Abell 496-2	4:33:42.9	−13:16:08	11.3	4.1	177 / 132	8±47
Abell 520-1	4:54:09.6	+02:54:48	3.7	3.3	166 / 177	0±13
Abell 520-2	4:54:06.8	+02:56:33	8.2	3.6	163 / 113	101±199
Abell 520-3[a]	4:54:09.5	+02:55:11	7.5	6.0	200 / 177	−1±21
Abell 586-1	7:32:17.6	+31:37:34	5.4	3.5	208 / 177	1±16
Abell 586-2[a]	7:32:19.5	+31:38:26	7.3	3.3	183 / 177	6±11
Abell 773-1	9:17:57.2	+51:42:30	7.7	3.8	172 / 177	−53±115
Abell 780-1	9:18:05.3	−12:05:41	69.3	17.1	185 / 135	75±58
Abell 851-1	9:42:55.5	+46:58:43	12.9	16.0	289 / 177	7±15
Abell 851-2	9:43:05.8	+46:58:33	4.5	3.3	186 / 177	39±27
Abell 851-3	9:43:05.1	+47:00:10	8.7	4.5	161 / 161	−32±140
Abell 851-4	9:42:53.1	+46:59:49	5.5	3.4	193 / 177	−2±13
Abell 851-5	9:42:48.4	+46:59:22	7.5	3.8	17 / 134	35±35
Abell 963-1	10:17:08.0	+39:02:59	4.7	4.5	212 / 177	−1±15
Abell 963-2	10:17:09.1	+39:03:37	8.5	5.1	196 / 177	23±41
Abell 963-3	10:16:57.2	+39:02:49	4.5	3.9	193 / 177	−14±57
Abell 963-4[a]	10:17:08.2	+39:02:25	4.6	3.7	218 / 177	3±17
Abell 1689-1	13:11:34.5	−01:20:20	7.2	6.4	190 / 177	9±28
Abell 1689-2[a]	13:11:29.2	−01:20:45	6.8	6.6	387 / 177	3±18
Abell 1835-1	14:01:04.7	+02:52:28	13.4	9.6	225 / 177	6±8
Abell 1835-2	14:00:57.5	+02:52:51	16.0	10.2	209 / 176	−2±13
Abell 1835-3	14:01:02.1	+02:52:43	4.5	4.1	160 / 177	1±6
Abell 2204-1	16:32:44.6	+05:34:54	16.8	4.8	175 / 177	5±72
Abell 2218-1	16:35:55.5	+66:12:58	6.2	8.7	384 / 177	2±25
Abell 2218-2	16:35:54.3	+66:12:30	10.8	23.5	187 / 177	14±17
Abell 2218-3	16:35:51.2	+66:12:07	4.8	8.7	401 / 177	8±29
Abell 2219-1	16:40:20.4	+46:44:01	9.6	5.3	189 / 177	−1±14
Abell 2219-2	16:40:23.9	+46:44:02	8.2	3.2	198 / 171	14±37
Abell 2390-1	21:53:33.2	+17:42:51	8.7	6.9	156 / 177	6±5
Abell 2597-1	23:25:19.8	−12:07:27	14.5	10.5	202 / 177	−2±14
Abell 2597-2	23:25:23.0	−12:07:52	6.6	3.4	156 / 177	2±10
Abell 2597-3	23:25:23.6	−12:06:51	6.7	3.8	190 / 171	−3±29
Cl 0016+16-1	00:18:29.3	+16:27:28	27.0	4.1	151 / 90	Off Edge
Cl 0016+16-2[a]	00:18:33.2	+16:26:10	5.5	3.7	199 / 177	−2±16
Cl 0023+0423-1	00:23:54.5	+04:23:03	5.9	5.7	155 / 177	13±24
Cl 0023+0423-2	00:23:53.5	+04:21:57	4.5	3.9	174 / 177	−10±29

Continued on next page

Table5 – continues from previous page

Cluster Source	α_{2000} (hh:mm:ss)	δ_{2000} (+dd:mm:ss)	850 μm Flux (mJy)	850 μm S/N	χ^2 / Degrees of Freedom	450 μm Flux (mJy)
Cl 0024+1652-1	00:26:34.0	+17:08:33	21.0	9.0	196 / 162	8±19
Cl 0024+1652-2[a]	00:26:37.5	+17:09:45	6.4	3.0	172 / 177	2±38
Cl 0848+4453-1	8:48:39.4	+44:53:47	6.0	4.1	177 / 177	−7±29
Cl 0848+4453-2	8:48:39.9	+44:54:22	10.8	6.6	173 / 177	10±52
Cl 0848+4453-3	8:48:31.7	+44:53:51	6.7	5.0	177 / 177	−14±31
Cl 1455+2232-1	14:57:16.2	+22:19:45	7.8	3.9	207 / 177	4±13
Cl 1455+2232-2[a]	14:57:16.0	+22:20:45	7.1	3.1	208 / 177	5±19
Cl 1604+4304-1	16:04:26.0	+43:03:57	4.9	4.4	163 / 177	12±20
Cl 1604+4304-2	16:04:22.7	+43:05:11	5.4	5.2	212 / 177	8±17
Cl 1604+4304-3	16:04:23.2	+43:05:29	6.2	4.2	230 / 177	−2±18
Cl 1604+4304-4	16:04:32.3	+43:04:23	12.0	3.6	124 / 111	Off Edge
Cl 1604+4304-5	16:04:30.1	+43:04:41	5.3	5.0	232 / 177	−3±17
Cl 1604+4304-6	16:04:28.8	+43:05:11	3.5	3.4	209 / 177	−6±18
Cl 1604+4304-7	16:04:29.2	+43:05:44	3.5	3.4	168 / 177	−10±29
Cl 1604+4304-8[a]	16:04:23.7	+43:04:40	8.2	9.0	212 / 177	18±20
Cl 2244−0221-1	22:47:13.8	−02:06:09	8.8	3.8	204 / 177	6±18
Cl 2244−0221-2	22:47:16.3	−02:05:48	4.6	3.3	197 / 167	2±21
Cl 2244−0221-3	22:47:12.3	−02:05:39	6.4	3.7	206 / 177	7±21
Cl 2244−0221-4	22:47:12.3	−02:04:25	6.5	3.1	148 / 131	Off Edge
Cl 2244−0221-5[a]	22:47:10.1	−02:05:57	9.0	6.0	174 / 177	6±28
MS 0440+0204-1	4:43:05.4	+02:10:35	5.0	3.1	161 / 177	−1±68
MS 0440+0204-2	4:43:06.8	+02:10:26	6.0	4.1	199 / 177	1±38
MS 0440+0204-3	4:43:14.6	+02:09:59	6.8	3.1	152 / 144	5±64
MS 0440+0204-4[a]	4:43:08.5	+02:10:37	4.2	3.4	211 / 177	−6±49
MS 0451−0305-1	4:54:09.2	−03:01:56	8.3	3.4	163 / 177	38±96
MS 0451−0305-2	4:54:07.1	−03:00:42	7.9	3.1	164 / 172	−1±94
MS 0451−0305-3	4:54:10.6	−03:01:24	10.6	5.4	200 / 177	−12±56
MS 0451−0305-4	4:54:12.8	−03:00:52	13.8	7.9	249 / 177	2±60
MS 0451−0305-5	4:54:15.6	−03:00:40	9.7	5.0	193 / 177	−20±73
MS 1054−0321-1	10:57:03.7	−03:37:12	5.9	4.5	190 / 177	3±13
MS 1054−0321-2	10:56:56.0	−03:36:34	5.3	4.1	152 / 177	15±26
MS 1054−0321-3	10:56:56.5	−03:36:11	6.2	5.7	163 / 177	25±37
MS 1054−0321-4	10:57:02.0	−03:36:06	6.0	4.4	180 / 177	15±21
MS 1054−0321-5	10:57:00.2	−03:35:39	5.0	4.1	201 / 177	31±20
RXJ 1347−1145-1	13:47:27.6	−11:45:54	15.1	5.1	140 / 177	125±34
RXJ 1347−1145-2[a]	13:47:31.3	−11:44:57	11.4	4.7	191 / 177	10±32

[a] These sources are possibly images of the SZ effect and we do not subtract them before doing the SZ effect fit. Because in an number of cases the apparent source is resolved, the χ^2 in some of these sources is poor.

APPENDIX C

This appendix contains notes on the characteristics of individual clusters, with emphasis on cm/mm/sub-mm and X-ray measurements of point sources and extended emission in each.

Abell 68: Cooray et al. (1998) has studied this moderate redshift cluster as part of a 28.5 GHz study of point sources in galaxy clusters.

Abell 85: This is a low redshift cluster with no apparent sub-mm point sources or extended emission. Measurements of the SZ effect in this cluster around 30 GHz have been published previously (Udomprasert et al. 2004, Baker et al. 1994).

Abell 209: This cluster is relatively poorly studied, particularly at (sub-)mm wavelengths.

Abell 222: This is a moderate redshift cluster with no apparent sub-mm emission, although the SCUBA map is quite shallow. Because the isothermal β model for this cluster had to be derived from archival X-ray data, it has not been considered a viable SZ effect field and has been removed from the analysis discussed in Section 3.3 and later.

Abell 370: This field contains the brightest source in this catalogue, discussed in detail in Ivison et al. (1998). Our results are consistent with those found by other groups (Smail et al. 1997, Barger et al. 1999). As shown in Grego et al. (2000), the SZ decrement shows quite complex structure in this cluster. LaRoque et al. (2006) provides a newer measurement of the SZ effect using OVRO/BIMA. Cooray et al. (1998) provides a point source list at 28.5 GHz for this cluster, and ISOCAM results at 14 and 7 μm have also been published (Metcalfe et al. 2003).

Abell 383: Cooray et al. (1998) provides a 28.5 GHz point source list for this moderate redshift cluster.

Abell 478: This cluster has been a popular target for SZ effect experiments; Radford et al. (1986) and Chase et al. (1987) discuss early attempts to measure the SZ effect at 3 and 1.2 mm, respectively. More recently, Myers et al. (1997) and Mason, Myers & Readhead (2001) discuss measurements of the SZ effect using OVRO at 32 GHz, Udomprasert et al. (2004) measures this cluster's SZ effect with CBI, and Lancaster et al. (2005) uses the VSA at 34 GHz as well.

Unfortunately, this cluster is a poor target for SZ effects at SCUBA's shorter wavelengths. Knudsen, van der Werf & Jaffe (2003) have presented the data discussed here and associate the bright point source near the centre of this field with a high redshift, dusty quasar. Previously, Cox, Bregman & Schombert (1995) discuss *IRAS* measurements of this cluster at 60 and 100 μm.

Pointecouteau et al. (2004) and de Plaa et al. (2004) discuss the X-ray properties of this cluster using recent *XMM-Newton* data, and Sun et al. (2003) presents similar measurements with *Chandra*.

Abell 496: This is a low redshift cluster, discussed extensively in Durret et al. 2000. We detect a bright source associated with the central galaxy in the cluster (Griffith et al. 1994). This cluster is therefore contaminated from the point of view of SZ effect measurement with the JCMT.

Abell 520: Chapman et al. (2002) provide a previous analysis of the sub-mm data for this cluster. The SZ effect has been measured at 30 GHz by Reese et al. (2002), with SuZIE II (Benson et al. 2004), and Cooray et al. (1998) provide a list of point sources at 28.5 GHz in this field.

Abell 586: A deep *XMM-Newton* observation is presented in De Filippis et al. (2003), and 28.5 GHz data focusing on point sources are given in Cooray et al. (1998). LaRoque et al. (2006) presents an SZ effect measurement at 30 GHz using OVRO/BIMA.

Abell 665: This moderate redshift cluster is another popular SZ effect target. Grego et al. (2001), Reese et al. (2002) and LaRoque et al. (2006) measure the SZ effect decrement at 30 GHz, and Cooray et al. (1998) measure point sources at the same frequency. Also, Desert et al. (1998) discusses DIABLO SZ observations at 2.1 and 1.2 mm.

Abell 773: The cluster has a number of SZ effect measurements. Benson et al. (2004) present measurement of the SZ effect using SuZIE II. Both Grainge et al. (1993), Saunders et al. (2003) and Jones et al. (2005) discuss a program of SZ effect measurements using the Ryle telescope. Also, Carlstrom, Joy & Grego (1996), Reese et al. (2002) and LaRoque et al. (2006) SZ effect measurements at 30 GHz in this cluster. Recently, Govoni et al. (2004) presented X-ray data from *Chandra* for this cluster.

Abell 780: Abell 780 contains Hydra A, an extremely bright radio source (AGN), in its central regions (Bennett et al. 2003). As Hydra A has a flux of about 0.1 Jy at 850 μm, it is not possible to isolate the SZ effect in this cluster.

Abell 851: Previous sub-mm measurements of this cluster are presented in Smail et al. (2002), while Cooray et al. (1998) present measurements of point sources at 28.5 GHz. De Filippis et al. (2003) find a complex X-ray structure in this cluster which exhibits two cores, each having a temperature of about 4.7 keV. We therefore expect that the isothermal β model is a poor description of the shape of the SZ effect emission in this cluster, and exclude it from the analysis discussed in Section 3.3.

Abell 963: This cluster is very well studied at optical wavelengths, and as a part of a number of X-ray surveys.

Abell 1689: Our map of Abell 1689 exhibits a great deal of extended sub-mm emission around the expected centriod of SZ effect emission, which is best explained as a sub-mm image of the cluster's SZ effect. This cluster has been a very popular target for SZ effect measurements, including SuZIE II (Benson et al. 2004) and OVRO/BIMA at the SZ decrement (Holzapfel et al. 1997, Grego et al. 2001, Reese et al. 2002, LaRoque et al. 2006). Cooray et al. (1998) discuss point sources at 30 GHz.

Abell 1763: Cooray et al. (1998) present point source measurements at 28.5 GHz for this cluster. Abell 1763 has been detected in a number of X-ray surveys.

Abell 1835: This field contains two known lensed sub-mm sources (Ivison et al. 2000) and has also been imaged at 1.1 mm with BOLOCAM (D. Haig, private communication). In addition, a small amount of emission in the central regions is detected at reasonable significance. Edge et al. (1999) associate this flux with dust emission from the central galaxy; this is supported by the detection of CO emission in this galaxy.

Grego et al. (2001) detect an SZ effect decrement at 30 GHz, and Cooray et al. (1998) discuss point sources detected at the same frequency. Mauskopf et al. (2000) and Benson et al. (2003) both find data consistent with a sub-mm SZ increment in this cluster using SuZIE I/II. Both Schmidt, Allen & Fabian (2001) and Majerowicz, Neumann & Reiprich (2002) present X-ray measurements of this cluster, finding a central ICM temperature of 4.0 and 4.4 keV, respectively. Abell 1835 has a strong cooling flow, and thus exhibits a temperature gradient between the centre and the hotter outer regions.

Abell 1914: This field only has about an hour of SCUBA integration time, resulting in a very shallow map. Grego et al. (2001) and LaRoque et al. (2006) give prior SZ effect measurements at 30 GHz, and Cooray et al. (1998) discuss point sources in this cluster. Also, Jones et al. (2005) use the Ryle telescope to measure the SZ effect in this cluster.

Abell 2163: This cluster is very well studied at mm wavelengths, particularly in terms of the SZ effect. SuZIE I/II has measured this cluster a number of times (Wilbanks et al. 1994, Holzapfel et al. 1997, Benson et al. 2004). Reese et al. (2002) and LaRoque et al. (2006) present SZ effect measurements at 30 GHz using BIMA/OVRO. The DIABOLO experiment has been used to measure the SZ effect in this cluster at millimetric wavelengths (Desert et al. 1998), and PRONAOS measured the sub-mm SZ effect for the first time in Abell 2163 (Lamarre et al. 1998).

Sadly, the SCUBA data for this cluster are pathologically noisy; the map shown in Fig.2 has structure that is not related to astronomical emission. We have attempted to understand this noise, but no obvious cause has been found. We therefore present the 850 μm map, but do not analyze the data beyond that stage.

Cooray et al. (1998) present 28.5 GHz point sources in this cluster, and Govoni et al. (2004) presents recent data from the *Chandra* observatory. Chapman et al. (2002) have discussed some of the SCUBA data presented in this work.

Abell 2204: The SZ effect in this cluster has previously been measured by Holzapfel (1996), Benson et al. (2004) and LaRoque et al. (2006), while Cooray et al. (1998) give a discussion of 28.5 GHz point sources in this cluster.

Abell 2218: This is among the best studied clusters in the sky, and is particularly popular for studies of gravitational lensing. In fact, one of the candidates for the highest redshift source ($z \simeq 7$) known is in this cluster field (Kneib et al. 2004a).

Kneib et al. (2004b) present the discovery of SMM J16359+6612, a high redshift, lensed sub-mm galaxy. This source is present in our maps, but because Kneib et al. (2004b) use a smaller pixel size, more structure is evident in their maps. This cluster is not used in our final SZ sample because the lensed source is too complex to model and remove from the data.

At wavelengths close to SCUBA's, Sheth et al. (2004) discuss the detection of CO from SMM J16359+6612, and Biviano et al. (2004) present an ISOCAM study of star forming galaxies in Abell 2218. Egami et al. (2005) presents *Spitzer* observations of this cluster as well. Cooray et al. (1998) list radio point sources at 28.5 GHz in this cluster.

Abell 2218 was also a popular target for early searches for the SZ effect like that presented in Radford et al. (1986) and culminating in work like that in Jones et al. (1993). More recently, this cluster has been imaged by the Effelsberg 100 m telescope at 10 GHz (Uyaniker et al. 1997), the Nobeyama telescope at 36 GHz (Tsuboi et al. 1998), SuZIE II (Benson et al. 2004), the Ryle telescope (Jones et al. 2005), and OVRO/BIMA around 30 GHz (Grego et al. 2001, Reese et al. 2002, LaRoque et al. 2006). It is not obvious that this cluster is a particularly good target for SZ observations above these frequencies due to SMM J16359+6612.

Recent X-ray studies of this cluster include Machacek et al. (2002) using *Chandra* and Pratt, Böhringer & Finoguenov (2005) using *XMM-Newton*.

Abell 2219: Chapman et al. (2002) provide a previous analysis of these sub-mm data, while Cooray et al. (1998) discuss 28.5 GHz point sources in this cluster.

Abell 2261: The SCUBA integration time on this cluster is only about 1.5 hours, resulting in a shallow map. Chapman et al. (2002) have presented a previous analysis of this sub-mm data. The SZ effect has been measured both at the decrement (Grego et al. 2000, Reese et al. 2002) and around the null (Benson et al. 2003, Benson et al. 2004). Cooray et al. (1998) discuss point source contamination near 30 GHz.

Abell 2390: These sub-mm data are discussed in Barger et al. (1999), and Edge et al. (1999), while Benson et al. (2003) provide a measurement of the SZ effect in this cluster using SuZIE II.

Abell 2597: Abell 2597 contains a bright AGN (Véron-Cetty & Véron 2001) which is imaged in this sub-mm data set. It is therefore not suitable for SCUBA SZ effect observations. Udomprasert et al. (2004) present a SZ effect study of this cluster using CBI.

Cl 0016+16: This cluster is probably the most popular SZ effect target in the sky; in addition to our previous work (Zemcov et al. 2003)[11], a number of experiments have measured the SZ effect in this cluster. Early measurements are discussed by Birkinshaw, Gull & Moffet (1981) and Birkinshaw, Gull & Hardebeck (1984). Benson et al. (2003) and Benson et al. (2004) discuss measurements using SuZIE II on the Caltech Sub-mm Observatory. Measurements using the OVRO/BIMA system around 30 GHz are discussed in Carlstrom, Joy & Grego (1996), Hughes & Birkinshaw (1998), Reese et al. (2000), Grego et al. (2001), Reese et al. (2002), LaRoque et al. (2003), and LaRoque et al. (2006). Desert et al. (1998) present SZ effect measurements using DIABOLO on IRAM, and Grainge et al. (2002) used the Ryle telescope for their SZ measurements.

Chapman et al. (2002) already presented an analysis of these sub-mm data, while Cooray et al. (1998) discusses measurements of radio point sources at 28.5 GHz in this cluster. This cluster has also been targeted with a number of X-ray telescopes; Worrall & Birkinshaw (2003) presents recent measurements using *XMM-Newton.*

Cl 0023+0423: This high z cluster was originally discovered in the survey of Gunn, Hoessel & Oke (1986). Best (2002) has previously analyzed these sub-mm data. As no isothermal β model parameters are available or derivable from archival data, an SZ effect measurement cannot be performed with these data.

[11] There are approximately 3 times more data in the work presented here than in Zemcov et al. (2003).

Cl 0024+1652: These SCUBA data have previously been discussed in Smail et al. (2002) and Frayer et al. (2000).

Cl 0055−2754: This is a relatively poorly studied cluster; due to both a lack of a well-defined SZ model, and the short integration time on this field, it has been rejected from our SZ sample. The map is presented in Fig. 2.

Cl 0152−1357: Maughan et al. (2003) discuss X-ray imaging of this cluster, and show that it is composed of two clumps. Our SCUBA data imaged the northern clump, which has an X-ray temperature of 5.5 keV. Joy et al. (2001) have previously measured the SZ effect in this cluster at 30 GHz.

Cl 0303+1706: This cluster is relatively poorly studied, particularly at mm wavelengths.

Cl 0848+4453: An analysis of these data has been presented previously by Best (2002).

Cl 1455+2232: Chapman et al. (2002) present a previous analysis of these sub-mm data, while Cooray et al. (1998) discuss a 28.5 GHz survey for point sources.

Cl 1604+4304: Gunn, Hoessel & Oke (1986) first detected a set of galaxy clusters in this region of the sky, and Lubin et al. (2000) showed that this cluster forms part of a larger supercluster with Cl 1604+4321. Best (2002) previously presented this sub-mm data. As the isothermal β model had to be estimated in this cluster, it has not been considered in the analysis presented in Section 3.3.

Cl 1604+4321: This is the partner of Cl 1604+4304 and the same comments apply.

Cl 2129+0005: This cluster hosts a bright AGN (Crawford et al. 1999), and so is not suitable for SCUBA SZ effect measurements.

Cl 2244−0221: Smail et al. (1997) present an analysis of the sub-mm emission in this cluster based on these SCUBA data. Ota et al. (1998) surveyed this region with *ASCA*, and find a best fitting isothermal model with $\beta = 0.30$. This value of β is physically acceptable for the X-ray emission, but produces a divergent model for the SZ effect. We therefore use the classic King profile ($\beta = 2/3$) for this cluster. However, this model has a very large core radius, and poorly describes these sub-mm data. As the model is such a poor description of the known properties of this cluster, we have not considered it in the analysis discussed in Section 3.3 and later.

MS 0440+0204: These SCUBA data have previously been presented in Barger et al. (1999) and Smail et al. (2002).

MS 0451−0305: This is a high redshift cluster in which Borys et al. (2004) have found a resolved, bright submm source. The same group presented a map made with some of these data earlier (Chapman et al. 2002), but did not have low enough noise to identify the source. While this source is interesting in its own right, it precludes the type of SZ analysis discussed in this paper.

This cluster is another popular target for SZ effect observations. It was discussed in our earlier work Zemcov et al. (2003), but was rejected from that SZ sample due to the lensed sub-mm source. Benson et al. (2003) and Benson et al. (2004) discuss observations of this cluster with SuZIE II. MS 0451−0305 is also a popular target for OVRO/BIMA at 30 GHz (Reese et al. 2000 Grego et al. 2001, Reese et al. 2002, LaRoque et al. 2003, LaRoque et al. 2006).

Cooray et al. (1998) describe a search for radio point sources at 28.5 GHz, and Donahue et al. (2003) presents recent *Chandra* maps for this cluster.

MS 1054−03: This is a high redshift, hot cluster of galaxies. It has been targeted for SZ effect observations by SCUBA (Zemcov et al. 2003), SuZIE II (Benson et al. 2004) and OVRO/BIMA (Joy et al. 2001, LaRoque et al. 2006). It is also well studied in the X-ray, most recently with *Chandra* (Jeltema et al. 2001) and *XMM-Newton* (Gioia et al. 2004).

Both Cooray et al. (1998) and Best et al. (2002) provide radio source lists for MS 1054−03. Chapman et al. (2002) previously discussed some of the data in the set presented here. A large fraction of the total integration time came later, and those data are presented in Knudsen et al. (2005); they present a deep source list, but not the map itself.

Some of the data for this cluster also appeared in Zemcov et al. (2003); the best fit SZ effect given there is consistent with that given in this work.

PKS 0745−19: Edge (2001) has presented this data as part of a programme to measure CO emission in galaxy clusters. Hicks et al. (2002) presents recent *Chandra* data for this cluster.

RXJ 1347−1145: RXJ 1347−1145 is the brightest cluster in the *ROSAT* sample; Allen, Schmidt & Fabian (2002) present measurement of this cluster with *Chandra*. They find a central X-ray temperature of 7.0 keV that rises to 16 keV away from the cluster centre.

This cluster has been a target for many SZ effect experiments from 30 GHz to 350 GHz (Komatsu et al. 1999, Pointecouteau et al. 1999, Pointecouteau et al. 2001, Komatsu et al. 2001, Reese et al. 2002, Benson et al. 2004, LaRoque et al. 2006). It exhibits what appears to be among the only images of the SZ effect at 350 GHz in our sample, although we find a different flux than that given by Komatsu et al. (1999).

RXJ 1347−1145 exhibits the only detected 450 μm source in this catalogue. Unfortunately, it is not clear what source this corresponds to at other wavelengths. Due to its proximity to the centre of the cluster, this source may be confused in SZ effect experiments with larger beams than that of SCUBA on the JCMT.

Zwicky 3146: These data have previously been analyzed and discussed by Chapman et al. (2002). The SZ effect has been measured by SuZIE I/II (Holzapfel 1996, Benson et al. 2003, Benson et al. 2004), while Cooray et al. (1998) discuss radio point sources at 28.5 GHz in this cluster.

This paper has been produced using the Royal Astronomical Society/Blackwell Science LaTeX style file.